Venus surface thermal emission at 1 mum in VIRTIS imaging observations: Evidence for variation of crust and mantle differentiation conditions

Nils T. Mueller, Jörn Helbert, G. L. Hashimoto, Constantine C. C. Tsang, Stéphane Erard, Giuseppe Piccioni, Pierre Drossart

Venus surface thermal emission at 1 μm in VIRTIS imaging observations: Evidence for variation of crust and mantle differentiation conditions

N. Mueller,[1] J. Helbert,[2] G. L. Hashimoto,[3] C. C. C. Tsang,[4] S. Erard,[5] G. Piccioni,[6] and P. Drossart[5]

Received 15 February 2008; revised 10 July 2008; accepted 20 August 2008; published 10 December 2008.

[1] The Venus Express spacecraft images the nightside thermal emissions using the Visible and Infrared Thermal Imaging Spectrometer (VIRTIS). At 1.02, 1.10, and 1.18 μm, thermal emission from the surface is observed. The signal is attenuated by scattering and absorption in the dense atmosphere. The measured flux at the top of the atmosphere is positively correlated with surface temperature and surface emissivity. The surface temperature of Venus is relatively well constrained as being mainly a function of altitude with a gradient lesser or equal to the adiabatic lapse rate. This study examines the correlation of VIRTIS images showing a signal of the surface at 1.02 μm with viewing geometry, stray sunlight, cloud opacity, and topography and applies semiempirical relations to remove their influence. The remaining contrast can be either ascribed to surface emissivity or unexpected temperature variations. Temperature variations due to active volcanism are unlikely to be persistent over the time of observations; therefore, the mosaic of all processed images is here interpreted in terms of surface emissivity variation. The emissivity variation found is correlated with geomorphological features established from Magellan synthetic aperture radar images. It is generally lower at tessera terrain. Some, but not all, volcanic edifices show increased emissivity. Large lava flows in the Lada terra-Lavinia planitia region also show an increased thermal emission. This might indicate a more felsic surface composition of tessera highlands and large-scale extrusive volcanism of ultramafic composition.

Citation: Mueller, N., J. Helbert, G. L. Hashimoto, C. C. C. Tsang, S. Erard, G. Piccioni, and P. Drossart (2008), Venus surface thermal emission at 1 μm in VIRTIS imaging observations: Evidence for variation of crust and mantle differentiation conditions, *J. Geophys. Res.*, *113*, E00B17, doi:10.1029/2008JE003118.

1. Motivation

[2] The search for exoplanets yields an ever increasing number of known planets. With further improvements in observation techniques it will hopefully soon be possible to detect Earth sized planets orbiting their stars at distances where liquid surface water is stable. The special interest in planets with these attributes is of course motivated by the desire to find habitable planets or even life. Size and orbital distance comparable to Earth is by no means an ideal indicator of habitability as the Earth's neighboring planets demonstrate. Venus with eight tenths of Earth's mass and nearly three fourths of Earth's orbital distance is quite inhospitable. The surface of Venus is extremely hot owing to greenhouse climate imposed by its dense CO_2 atmosphere and sulfuric acid clouds. Surface and atmosphere are also dry compared to Earth [*Taylor*, 2006].

[3] Comprehensive understanding of why Venus so utterly failed to become remotely habitable has not yet been achieved [*Crisp et al.*, 2002]. One missing piece for the reconstruction of the evolution of Venus is global knowledge on the composition of the crust. The surface has been extensively mapped at radar wavelengths by the Magellan mission [*Pettengill et al.*, 1991] which further revealed a unique geology [e.g., *Saunders et al.*, 1991; *Head et al.*, 1992; *Solomon et al.*, 1992; *Schaber et al.*, 1992; *Phillips et al.*, 1992; *Stofan et al.*, 1992, 1997; *Hansen et al.*, 1997; *Smrekar et al.*, 1997; *Grimm and Hess*, 1997; *Basilevsky et al.*, 1997]. Radar is however not very sensitive to mineral composition. The discovery of spectral windows in the atmosphere (Figure 1) that allow measurable amounts of near-infrared thermal emission from the surface to escape [*Carlson et al.*, 1991] presents the opportunity for limited remote sensing of surface mineralogy [*Carlson et al.*, 1993a; *Lecacheux et al.*, 1993; *Baines*

[1]Joint Planetary Interior Physics Research Group of the University Muenster and DLR Berlin, Berlin, Germany.
[2]Institute of Planetary Research, DLR, Berlin, Germany.
[3]Laboratory for Earth and Planetary Atmospheric Science, Department of Earth and Planetary Sciences, Kobe University, Kobe, Japan.
[4]Atmospheric, Oceanic, and Planetary Physics, Department of Physics, Clarendon Laboratory, University of Oxford, Oxford, UK.
[5]LESIA, Observatoire de Paris, Paris, France.
[6]IASF-INAF, Rome, Italy.

0148-0227/08/2008JE003118

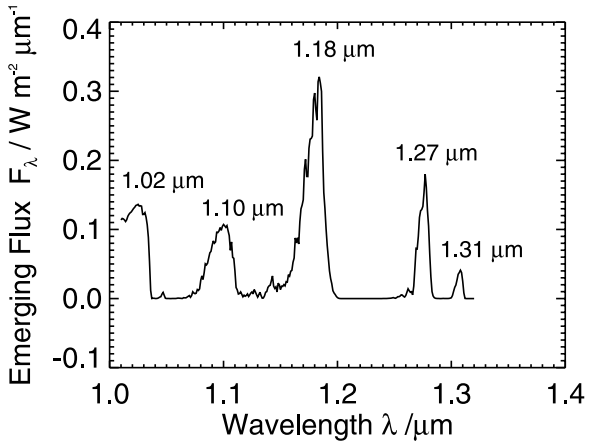

Figure 1. Modeled spectrum of the near-infrared (NIR) windows at VIRTIS-H spectral resolution [*Drossart et al.*, 2007]. Model is described by *Tsang et al.* [2008]. The different windows feature different amounts of emission originating from the surface: at 1.02 μm more than 95% comes from the surface, and at 1.27 and 1.31 μm a negligible part of the radiation comes from the surface [*Meadows and Crisp*, 1996].

et al., 2000; *Moroz*, 2002; *Hashimoto and Sugita*, 2003; *Hashimoto et al.*, 2008; *Arnold et al.*, 2008; A. T. Basilevsky et al., Geologic interpretation of the near-infrared images of the surface taken by the Venus Monitoring Camera, Venus Express, submitted to *Journal of Geophysical Research*, 2008].

[4] The window most suited for this purpose is at 1 μm which coincides with a absorbtion band of FeO, one of the primary compounds of mafic minerals. Abundance of refractory mafic minerals gives evidence of the conditions under which the ultramafic mantle material differentiated and formed the crust. It is possible to distinguish three different types of crustal differentiation [*Taylor*, 1989]. Primary differentiation is the formation of floating crust in a fully molten mantle or magma ocean. Evidence for this is found in the lunar highland anorthosite rocks returned by the Apollo missions [*Taylor*, 1974]. Secondary differentiation occurs when the convecting mantle material partially melts, the liquid phase moves upward and forms a basaltic crust either by volcanism or plutonic intrusion, e.g., at mid-ocean ridges on Earth. Tertiary differentiation requires recycling of basaltic crust and water into the mantle. Water lowers the liquidus temperature of secondary crust which creates partial melts with a felsic composition that generated the bulk of the continental crust on Earth [*Taylor and Campbell*, 1983]. The greater part of the venusian crust is thought to be formed by secondary differentiation [*Head et al.*, 1994; *Grimm and Hess*, 1997]. Arguments for this are lava viscosity inferred from morphology, in situ measurements and the unimodal hypsometry. Most in situ measurements indicate a mafic composition comparable to common terrestrial basalts [*Surkov and Barsukov*, 1985; *Surkov et al.*, 1986, 1987]. Two out of seven, Venera 8 and Venera 13, indicate a more complex differentiation process that involves enrichment in abundance of alkalines [*Kargel et al.*, 1993]. Abundance of alkalines is not reflected in the felsic-mafic description.

[5] Crustal differentiation is counteracted by thermal buoyancy, which on Earth leads to remixing of crustal material into the mantle by oceanic plate subduction. It is not very well constrained whether crustal recycling takes or took place on Venus [*Grimm and Hess*, 1997]. Crater frequency gives strong evidence for relative recent resurfacing [*Phillips et al.*, 1992; *Schaber et al.*, 1992; *Strom et al.*, 1994]. The crust mapped by radar appears young because extrusive volcanism and tectonic deformation have erased the early crater history. The processes responsible for the resurfacing are not fully understood, and the fact of a seemingly young crust does not constrain crustal recycling. For instance, the concept of episodic plate tectonics [*Turcotte*, 1993] involves recycling of most of the crust and simultaneous creation of new crust. In other models considering vertical rather than horizontal accretion [e.g., *Parmentier and Hess*, 1992; *Head et al.*, 1994], recycling takes place only if crustal growths exceeds a thickness of 60 to 80 km and crustal basalt minerals undergo a phase transition to denser eclogite [*Spohn*, 1991]. Mapping of geochemically old crust (i.e., granite or anorthosite) might constrain rate of crustal formation and recycling.

[6] Another product of mantle differentiation is the silica and FeO depleted material remaining in the mantle after the liquid basaltic phase migrated upward. *Parmentier and Hess* [1992] assume that this residual material forms a compositionally buoyant layer below the crust. On Earth this reservoir is thought to be small owing to lithosphere subduction. On Venus plate tectonics is not unambiguously identifiable [*Kaula and Phillips*, 1981; *Solomon et al.*, 1992], and the lithosphere is assumed at present to form a stagnant lid [*Solomatov and Moresi*, 1996]. The reservoir of depleted mantle material on Venus is therefore likely greater than on Earth and steadily increasing during secondary differentiation as it is not remixed into the mantle by subduction. Cooling of this conducting layer leads to negative net buoyancy and foundering of the layer drives episodic tectonic and volcanic resurfacing. In the context of this resurfacing model, *Head et al.* [1994] predict composition of lava to be of ultramafic, e.g., picritic or komatiitic composition during the periods of quiescence as partial melting in mantle diapirs occurs in deeper regions under different conditions.

[7] Regardless of the stagnant lithosphere the surface is strongly influenced by endogenous processes. Mantle diapirs supposedly lift the volcanic dome shaped highlands through dynamic support and lithosphere thinning and imprint coronae structures [*Smrekar et al.*, 1997; *Stofan et al.*, 1997]. The wide range of topographic expressions of coronae can be explained by mantle diapirism triggering a gravitational instability and delamination of lithosphere [*Smrekar and Stofan*, 1997]. Lithosphere delamination can also account for the wide range of inferred lava viscosities requiring a diversity of melt compositions [*Elkins-Tanton et al.*, 2007]. Their modeling of the temperature-pressure conditions in and around a diapir of delaminating lithosphere demonstrates the possibility of generation of melt varying in SiO_2 abundance from 60% (intermediary between felsic and mafic) to 40% (ultramafic).

[8] The process of differentiation and recycling of crustal material is relevant for the thermal evolution of the interior of the planet. One side is the effective cooling of the interior

by recycling of cool crustal material. The other side is the distribution of radioactive heat sources throughout the planet. Important radioactive heat sources such as ^{40}K, ^{140}Th, and ^{239}U are incompatible, during partial melting these isotopes are enriched in the liquid, more felsic phase. Thus, on Earth the oceanic basaltic and especially the continental granitic crust contain higher abundances of radioactive elements than the mantle. This concentration of heat sources toward the top decreases the heat flux in the deep interior of the planet and also influences amount of magmatism by depletion of mantle heat sources [*Spohn*, 1991].

[9] The convective heat flux in the outer core driven by overall cooling of the planet is the energy source for the magnetic field of the Earth and presumably Mercury [*Stevenson et al.*, 1983]. The geodynamo process is currently not active on Venus but it is conceivable that it was in the past when distribution of the radioactive elements or the cooling of the planetary interior by lithosphere recycling was different. An intrinsic magnetic field would greatly influence the process of atmospheric erosion and allow Venus to retain its primordial water longer [*Donahue and Russell*, 1997]. In such an primordial climate and tectonic regime tertiary differentiation might have occurred and led to granitic cratons still existing in the Venusian highlands [*Taylor and Campbell*, 1983]. *Hashimoto and Sugita* [2003] concluded that it is possible to distinguish mafic basalt from felsic granite or rhyolite from orbit when given a sufficient but not impossible accuracy of measurement of thermal emission on the nightside of Venus.

[10] The aim of this study is to analyze VIRTIS images to find whether there is a spatial signal that can be plausibly attributed to content of mafic minerals of the topmost crust in the context of surface morphology from Magellan synthetic aperture radar (SAR) images.

2. Background and Theory

2.1. Atmosphere and Surface Temperature

[11] The thermal emission is dominated by surface temperature T as it is at any wavelength λ the product of surface emissivity ε_λ and blackbody spectral radiance given by the Planck function $B_\lambda(T)$. At the wavelengths and temperatures relevant here (1 μm and 735 K) the Planck function varies strongly with temperature. To retrieve surface emissivity from remote sensing of the thermal emission, the physical surface temperature must be well known. On Venus atmospheric temperature is well constrained owing to the insulating greenhouse climate and measurements at different local times and locations by the Venera, Pioneer Venus, and Vega descent probes. The surface temperature is thought to be in thermal equilibrium with the atmosphere owing to high heat capacity of the atmosphere and little diurnal variations [*Lecacheux et al.*, 1993].

[12] *Stone* [1975] estimated the different time scales of radiative heating and cooling and convective heat transport of the atmosphere of Venus and concluded that temperature was governed by the latter. Change of temperature by solar heating and cooling during the night is effectively distributed through the whole atmosphere by advection. Average diurnal and meridional temperature variations in the lower atmosphere were estimated to be less than 0.1 K.

[13] The in situ measurements of Venera 9 to 11 and the four Pioneer Venus descent probes reviewed by *Seiff* [1983] agree with each other within approximately 12 K at the same pressure level in the atmosphere below the clouds. The temperature increases toward the surface close to the adiabatic gradient. Diurnal variations are less than 1 K and latitudinal variations are less than 5 K in the data from the Pioneer Venus probes.

[14] Observations combined with atmospheric models lead to the Venus International Reference Atmosphere (VIRA). The model temperature structure is presented by *Seiff et al.* [1985]. The atmosphere in contact with the surface close to the mean planetary radius has a temperature of 735.3 K at 92.1 bar, adiabatical lapse rate is -8.06 K km^{-1}, no diurnal or latitudinal variations are included in the model atmosphere.

[15] Little is known however about the planetary boundary layer of the atmosphere since Venera probes were designed to travel through the hot atmosphere at great speed to maximize lifetime on the surface and the vertical temperature sampling rate is low. The higher-resolution measurements of the Pioneer Venus probes ceased at 12 km height. The Vega 2 temperature profile is the only measurement in the lower part of the atmosphere comparable in resolution to Pioneer Venus measurements. It shows a stratified atmosphere with dynamically unstable superadiabatic lapse rates in the lowest 6.5 km [*Seiff*, 1987]. In the lowest 1.5 km the lapse rates vary between -1.5 and -10 K km^{-1}. These measurements are not verified and no explanation for them has been found yet [*Crisp and Titov*, 1997]. Theoretical consideration by *Gierasch et al.* [1997] of the planetary boundary, where vertical convective motion is inhibited by the surface of the planet, gives an upper estimate of a diurnal temperature oscillation of 6 K corresponding to a 170 m thin thermal boundary layer.

[16] In conclusion, the small variation of temperature in the lowest layer of the atmosphere is well constrained but the temperature structure is not. The single high-resolution in situ measurement points toward possible superadiabatic lapse rates near the surface but is on average -8 K km^{-1}. Temperatures retrieved from observation of the thermal surface emission at 1.18 μm via radiative transfer modeling suggest a subadiabatic lapse rate of less than -7.5 K km^{-1} [*Meadows and Crisp*, 1996]. Measurement variations and theoretical diurnal variations near the surface are both less than 10 K at the same pressure level. The atmospheric boundary layer is probably not very relevant for the nightside owing to the long duration of nights on Venus (58 Earth days). No significant near-infrared (NIR) thermal emission variation with local time or latitude has been reported by *Lecacheux et al.* [1993], *Meadows and Crisp* [1996], or *Hashimoto et al.* [2008].

2.2. Radiative Transfer in the Atmosphere of Venus

[17] The atmosphere of Venus consists mostly of CO_2 (96.5 wt %) and N_2 (3.5 wt %) [*von Zahn et al.*, 1983] with a pressure of 93.2 bar at the zero altitude mean planetary radius (MPR) [*Seiff et al.*, 1985]. From approximately 50 to 70 km above MPR there are several cloud layers composed mostly of droplets of concentrated sulphuric acid. The clouds have spatially varying number densities and size distributions resulting in optical depths between 30 and

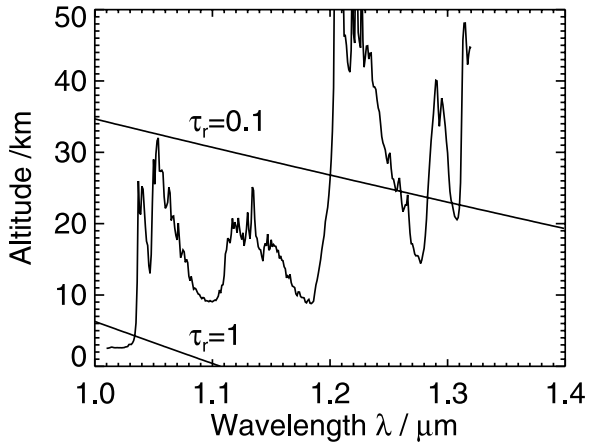

Figure 2. The altitude where brightness temperature of the lower atmosphere without clouds corresponds to atmospheric temperature gives an approximation for the source region of radiation. Spectrum calculated from the same model as in Figure 1 but without clouds. Isolines of Rayleigh scattering optical depths τ_r calculated following *Hansen and Travis* [1974]. Rayleigh scattering is less relevant for the 1.31 μm window than for the 1.02 μm window. Brightness temperature varies little between 1.01 and 1.03 μm in this model with a constant continuum absorption coefficient. Compare with spectral dependance of brightness temperature in Figure 8.

50 at visible wavelengths, for a review see *Ragent et al.* [1985]. A three modal size distribution with modal radii of 0.3, 1.0, and 3.7 μm is well established from in situ and remote observations [*Hansen and Hovenier*, 1974; *Marov et al.*, 1980; *Knollenberg and Hunten*, 1980; *Carlson et al.*, 1993b; *Grinspoon et al.*, 1993], but it is unclear whether this is a comprehensive description of all cloud particles. In particular the nature of the UV absorber leaving distinct cloud shaped marks on dayside images is not known [*Esposito et al.*, 1997]. Also, for mode 1 and 3 particles, compositions different from H_2SO_4 solutions and including solid crystals have been proposed [*Ragent et al.*, 1985; *Esposito et al.*, 1997]. In clouds models usually a mode 2′ is included that features a slightly larger modal radius and size variation than mode 2. Above and below the clouds are haze layers of mostly submicrometer particles. Hazes below the clouds have a total optical depth of less than 3 [*Ragent et al.*, 1985] that, however, might have been as high as 10 in Venera 8 near terminator measurements [*Moroz*, 2002]. *Ragent et al.* [1985], reviewing the different in situ measurements of hazes, gives no information for altitudes below 10 km. *Grieger et al.* [2004] reexamined the zenith and nadir radiance measurements of Venera 13 and Venera 14 and found in both a distinct peak of extinction between 1 and 2 km that they concluded to be a near surface cloud deck or haze layer.

[18] In conclusion, the atmosphere is optically thick at all visible and infrared wavelengths. Light scattering in the clouds and hazes prohibits direct or indirect surface observation in visible light. Scattering is conservative [*Ragent et al.*, 1985] which allows a small fraction of incident sunlight to reach the surface [see, e.g., *Gierasch et al.*, 1997]. Most sunlight is reflected at the cloud layer but Rayleigh scattering in the deep atmosphere is also not negligible [*Sagan*, 1962; *Moroz*, 2002]. Sunlight reflected from the surface is not significantly distinguishable against this background down to an altitude of 2 km at 0.65 μm [*Moroz*, 2002]. Figure 2 shows altitudes of Rayleigh scattering optical thicknesses 0.1 and 1 in the wavelengths studied in here.

[19] In the infrared range beyond 2.5 μm gases and H_2SO_4 cloud particles become strongly absorbing, thermal emission corresponds approximately to the temperatures of the cloud tops. The average brightness temperature of Venus in this range is 220 to 250 K on both dayside and nightside [*Pettit and Nicholson*, 1955; *Moroz et al.*, 1985] which corresponds to atmospheric temperature at 60 to 75 km height [*Seiff et al.*, 1985]. In the near infrared region there are several windows between CO_2 and H_2O absorption bands that allow measurable thermal emission from deeper layers to escape. The emissions from these windows were first discovered by *Allen and Crawford* [1984] at 1.74 μm and 2.30 μm. On the basis of shape, distribution, and revolution period of the bright and dark markings they concluded the observable contrast to be due to the illumination of the variable lower cloud layer by thermal emissions of the hot matter below the clouds. *Kamp et al.* [1988] found the emitting matter at these wavelengths to be CO_2 in the deep atmosphere. Absorption/emission increases with depth owing to higher density and pressure and temperature broadening of absorption bands. On the basis of their calculations they predicted further windows in the 1 μm region that were subsequently observed at 1.10 μm, 1.18 μm, 1.27 μm and 1.31 μm by ground-based observations [*Crisp et al.*, 1991] and during the Galileo flyby [*Carlson et al.*, 1991] at 1.2 μm, 1.01 μm, and 0.8 μm. Two more windows were observed by Cassini VIMS at 0.85 μm and 0.9 μm [*Baines et al.*, 2000].

[20] In addition to the cloud like markings simultaneously seen in all window regions, in those shortward of 1.2 μm the contrast of the thermal emission of cold highlands and hot lowlands is observed [*Crisp et al.*, 1991; *Carlson et al.*, 1993a]. *Lecacheux et al.* [1993] investigated this contrast in ground-based observations of the 1.02 μm window. Using a radiative transfer model they found the contrast correlated with surface elevation to be consistent with thermal emission of the surface in thermal equilibrium with the atmosphere and less than 10% variation in emissivity.

[21] One obstacle in modeling of the windows into the lower atmosphere of Venus is that little or no laboratory data exist on gaseous absorption at comparable pressures and optical paths. In spectral window regions far from absorption bands, absorption coefficients cannot fully be determined from existing absorption line databases and standard line shapes [*Taylor et al.*, 1997]. Parameters describing the continuum absorption are often determined empirically, i.e., chosen such that modeled spectra best fit the observed spectra [see, e.g., *Pollack et al.*, 1993; *Meadows and Crisp*, 1996; *Marcq et al.*, 2006; *Tsang et al.*, 2008].

[22] The optical properties of the clouds are better understood and consistent with Mie scattering at spheres with the refractive index of 75 wt % solution of H_2SO_4 [e.g., *Hansen and Hovenier*, 1974; *Grinspoon et al.*, 1993; *Pollack et al.*, 1993; *Carlson et al.*, 1993b]. On the basis of imaging observations of the windows at 1.74 μm and 2.30 μm with

Galileo NIMS *Carlson et al.* [1993b] attributed the cloud contrast not only to varying particle number densities but also to a shift in size or modal distribution. *Grinspoon et al.* [1993] calculated the scattering properties of cloud particles using Mie theory. Subsequent radiative transfer modeling yielded best results to NIMS data by variation of modes 2' and 3 in the middle and lower clouds, confirming the findings of *Carlson et al.* [1993b].

[23] Figure 1 shows a synthetic spectrum of the nightside of Venus based on gaseous absorption line databases and Mie scattering calculations for cloud particles as sulfuric acid droplets. The model is described by *Tsang et al.* [2008], with surface emissivity 0.8, surface temperature 740 K, a continuum absorption coefficient of 3.0×10^{-9} $cm^{-1}amagat^{-2}$, cloud model from *Pollack et al.* [1993], and no subcloud haze.

[24] In windows shortward of 1.74 μm, cloud particles scatter almost conservatively. Single scattering albedos differ from unity less than 10^{-3} in magnitude [*Grinspoon et al.*, 1993, Figure 1d]. Subsequently, cloud optical properties are approximately the same at the wavelengths of these windows. *Meadows and Crisp* [1996] exploit this to diminish cloud contrast in imaging observations via the ratio of surface windows (1.02, 1.10, and 1.18 μm) to the atmospheric window at 1.31 μm. At 1.31 μm the atmosphere becomes strongly absorbing between clouds and surface. Atmospheric brightness temperature can assumed to be horizontally constant below the clouds wherefore observable contrast of flux at top of atmosphere gives local transmittance of flux through the clouds. To interpret thus "declouded" images, *Meadows and Crisp* [1996] construct a synthetic image based on their model of the transfer of surface thermal emission. Temperatures were calculated from Pioneer Venus altimetry and a uniform emissivity of basalt (0.85) was chosen. The ratio of synthetic to declouded observed image showed less than 10% variation which is presented as upper limit of surface emissivity variation at 1.18 μm. There is still a slight negative correlation with the cloud contrast to be seen in the declouded image. Additionally, for the effect of topography or surface temperature to vanish in emissivity, a lapse rate with 7.5 K km^{-1} has to be chosen, which is different from the 8.06 K km^{-1} given by the VIRA model [*Seiff et al.*, 1985].

[25] As *Moroz* [2002] and *Hashimoto and Sugita* [2003] point out, this approach employing simple ratios to account for cloud and topography contrast neglects, that emerging flux at a surface window is neither proportional to surface emissivity nor to the cloud transmittance determined from 1.31 μm because of the different lower boundary conditions. While at 1.31 μm the deep atmosphere below the clouds reflects no downwelling radiation, at 1.02 μm atmospheric absorption is small enough for multiple reflections between atmosphere and surface to be relevant for emerging flux. Because cloud reflectivity and surface albedo are negatively correlated to cloud transmittance and surface emissivity, respectively, the contrast of emerging flux that contains significant contribution from multiple reflections is diminished compared to the direct proportionality implicitly assumed by *Meadows and Crisp* [1996]. *Hashimoto and Sugita* [2003] conclude that the slight negative correlation with cloud contrast in the emissivity presented by *Meadows and Crisp* [1996] is likely due to this effect and also that actual variation of emissivity might be higher than reported by *Meadows and Crisp* [1996]. *Hashimoto and Sugita* [2003] also employ a two-stream approximation to quantify the effect of multiple reflections and to study the observability of the surface emissivity from orbit. This approximation is here adapted to parameterize the effect of the atmosphere on the emerging thermal emission at 1.02 μm.

2.3. Atmosphere Parametrization

[26] *Moroz* [2002] and *Hashimoto and Sugita* [2003] give an approximation for the relation between surface thermal emission flux F_λ^{therm} and emerging flux F_λ at the top of a highly reflective atmosphere

$$F_\lambda = \frac{t}{1 - a_\lambda r} F_\lambda^{\text{therm}} \tag{1}$$

where t is transmission of the atmosphere, r is reflectivity of atmosphere and a_λ is lower boundary albedo. Equation (1) is exact for plane parallel conservative atmospheres which is approximately true for atmospheric layers composing the clouds at the window wavelengths and it is $t = 1\text{-}r$. *Hashimoto and Sugita* [2003] assume that cloud reflectivity r is the same for both surface window and the atmospheric window at 1.31 μm.

[27] $F_{1.31\mu m}^{\text{therm}}$ is constant because the atmosphere becomes opaque owing to absorption and emits in local thermal equilibrium with the constant atmospheric temperature. Brightness of the thermal emission from radiative transfer modeling [*Tsang et al.*, 2008] gives a rough approximation for the height of the transition from a conservative to absorbing atmosphere and thus for the source region of radiation (Figure 2), for a better estimate see the contribution functions by *Tsang et al.* [2008]. The isoline of $\tau_r = 0.1$ in Figure 2 illustrates that Rayleigh scattering is not very important in the source region of the 1.31 μm window at approximately 20 km height. Little downwelling radiation is scattered upward in the source region; this allows us to assume $a_{1.31\mu m} = 0$ [*Hashimoto and Sugita*, 2003]. Equation (1) then becomes

$$r = 1 - \frac{F_{1.31\mu m}}{F_{1.31\mu m}^{\text{therm}}} \tag{2}$$

and allows us to calculate to calculate the atmospheric reflectivity r above the source region of the 1.31 μm window.

[28] Cloud reflectivity r contains all required information on the variable cloud transmittance and can be used to remove cloud contrast at 1.02 μm with equation (1). Cloud reflectivity r does not account for scattering below the source region of the 1.31 μm window, however there is significant scattering at 1.02 μm below 35 km due to Rayleigh scattering (Figure 2) and possibly due to aerosols [*Moroz*, 2002; *Grieger et al.*, 2004]. Additionally, there is some small but poorly constrained amount of gaseous absorption due to the high pressure. Therefore, the parameters a_λ and F_λ^{therm} do not directly represent the surface in the frame of equations (1) and (2), but rather a composite of surface and lowest atmosphere that cannot be disentangled

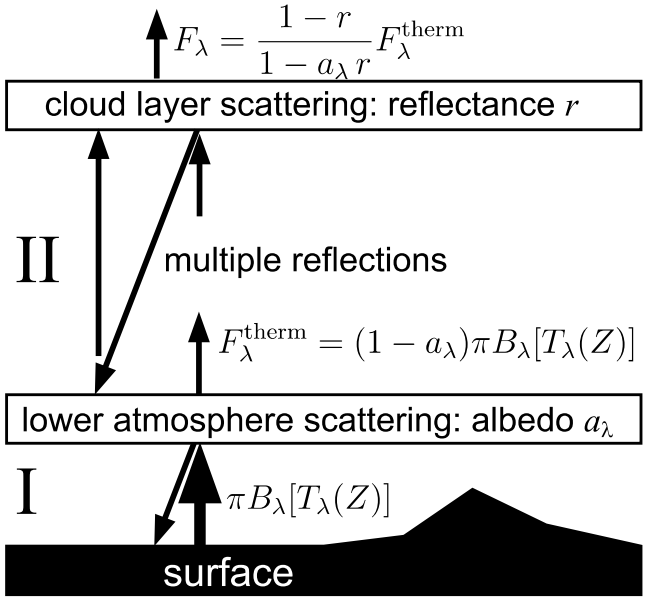

Figure 3. Sketch illustrating the atmosphere parametrization. Layer 1 is the lowest part of the atmosphere, from the surface to ~35 km altitude. Its average behavior, including the surface, is described empirically. Source of thermal radiation is assumed to be a blackbody emitting flux $\pi B_\lambda[T_\lambda(Z)]$; scattering in the lowest atmosphere is represented by a_λ. Layer 2 is the atmosphere from 35 km to the top of the atmosphere, which is approximately conservative and grey. This allows us to account for the cloud contrast at 1.02 μm using the VIRTIS images at 1.31 μm to determine cloud reflectivity r. Deviation of data from top of atmosphere flux derived using this model may indicate surface temperature or emissivity anomalies.

easily. Instead, global average behavior of these two parameters is determined empirically from VIRTIS data in section 4.4.

[29] For a better understanding of the parameters a_λ and $F_\lambda^{\mathrm{therm}}$, consider an additional atmospheric layer (Figure 3, layer 1) below the part of the atmosphere that is spectrally grey and conservative (Figure 3, layer 2). There is no evidence for horizontal variation in optical properties other than surface topography Z in this layer. Surface topography affects extinction optical depth but also determines average surface temperature. For sake of simplicity, the surface is represented by a blackbody with hemispherically integrated thermal emission $\pi B_\lambda[T_\lambda(Z)]$, with a temperature term $T_\lambda(Z)$ that encompasses all brightness variations due to topography. Topography-independent scattering is represented by a_λ. When conservative scattering is assumed, this allows us to rewrite equation (1):

$$F_\lambda = \frac{(1-r)}{1-a_\lambda r}(1-a_\lambda)\pi B_\lambda[T_\lambda(Z)] \tag{3}$$

$T_\lambda(Z)$ is an approximation for surface temperature. This approximation deviates from real surface temperature owing to absorption, multiple reflections within the lowest atmosphere, and the dependance of optical depth on topography Z. In reality, a_λ will depend on surface topography too, but Figure 7 shows that a constant a_λ is consistent with the data and a certain fit of $T_\lambda(Z)$.

[30] Equation (3) relates the observable flux F_λ to three parameters, upper atmosphere reflectivity r, lowest atmosphere and surface reflectivity a_λ, and temperature parameter $T_\lambda(Z)$, none of which is directly indicative of surface composition. Since surface composition variability is the aim of this study, equation (3) has to be interpreted in light of the implicit assumption of no surface emissivity variability. Any local deviation of VIRTIS data from the solution of equation (3) with empirically found values for the three unknown parameters is related either to local variations in the properties of the atmosphere or, since there is yet no evidence for such variations, to surface properties. To quantify this deviation, VIRTIS data are introduced as F_λ and thermal flux anomaly A_λ is defined as deviation from unity of the ratio of both sides of equation (3)

$$A_\lambda = 1 - \frac{F_\lambda(1-a_\lambda r)}{(1-r)(1-a_\lambda)\pi B_\lambda[T_\lambda(Z)]} \tag{4}$$

Surface emissivity is positively correlated with A_λ, but surface temperature variation not expressed by $T_\lambda(Z)$ also affects it.

3. Surface Observations by VIRTIS on Venus Express

[31] The VIRTIS instrument on Venus Express is a flight spare of the instrument of the same name of the Rosetta mission [*Drossart et al.*, 2007]. The versatility of the instrument originally designed to observe coma and nucleus of a comet at moderate spectral and spatial resolution [*Coradini et al.*, 1998] allows imaging of all NIR windows longward of 1 μm wavelength from Venus orbit. The infrared mapping subsystem VIRTIS-M IR that acquired the data for this study diffracts a light bundle selected by a slit with on a detector array. Data sets acquired at a given time (frames) therefore have one spatial and one spectral dimension, here referred to as samples and bands with index b. The detector array has 256 samples and 431 bands, in total giving a field of view of 64 mrad, corresponding to approximately a third of the diameter of Venus at apocenter, and a spectral range from approximately 1 μm to 5 μm. A scanning mirror with 256 position allows the instrument to construct hyperspectral image cubes by appending frames acquired consecutively at different viewing angles, thus adding a third dimension of lines. Neither mission nor instrument are specifically designed to observe the thermal emission of the surface but the manifold objectives of the mission requires different viewing geometries and integration times [*Svedhem et al.*, 2007]. The signals of the surface temperature and moreover of surface emissivity are small compared to the reflected sunlight on the dayside and require several seconds of exposure on the nightside to gain sufficient signal-to-noise ratio (SNR). Additionally a correction for variable cloud opacity such as attempted here is an additional source of noise that is especially critical since radiance and SNR at 1.31 μm is even lower. The error in cloud reflectivity derived from 1.31 μm is a major contribution to overall uncertainty in retrieval of surface properties [*Hashimoto and Sugita*, 2003]. There is an atmospheric

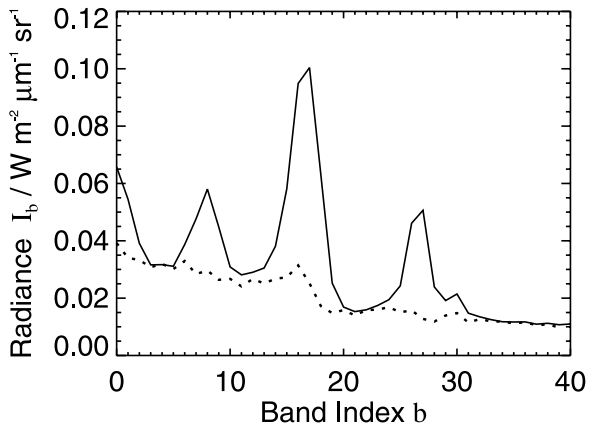

Figure 4. VIRTIS data spectrum from cube VI0112_01, line 0, sample 0. Dotted line is stray light spectrum S_b scaled to fit radiance $\overline{I_{[36,39]}}$. Stray light is removed by subtraction of individually scaled stray light spectra from all data spectra, similar to the approach by *Meadows and Crisp* [1996].

window at 1.27 μm with comparable properties and better SNR. Unfortunately it is coincident with oxygen airglow in the upper atmosphere [*Crisp et al.*, 1996] and unsuitable for a straightforward determination of cloud transmittance. The long duration of the mission and repeated observations of the same area of surface gives the unprecedent opportunity to combine observations over a long period of time to enhance the time invariant signal of the surface and to offset the poor SNR.

[32] The 24 h eccentrical polar orbit with pericenter at approximately 80°N exclusively allows for imaging of the southern hemisphere. Science planning of the mission is described by *Titov et al.* [2006]. Observation schemes are designated as science cases. All relevant cases are briefly summarized here: The northern hemisphere is only accessible in case 1 observations that are composed of isolated lines of spectra perpendicular to the spacecrafts track. Case 3 observations are apocenter mosaics of either the entire visible southern hemisphere or alternatively of either dayside or nightside. Owing to the eccentrical polar orbit these observations show the equatorial regions only at very high emission angles and accordingly low spatial resolution. Case 2 observations are done on the ascending or descending branch of the orbit and therefore able to observe regions up to 30°S with fairly low emergence. During most observations, especially case 3, nadir is at low latitudes and on average observed latitude is correlated to emission angle. At low latitudes the terminator is in or close to the field of view and observations are affected by sunlight scattered in the upper atmosphere and instrumental stray light originating from the bright side of Venus. In addition to the viewing geometry affecting the measured radiance, there is a shift from observation to observation in band positions due to varying thermal strain in the instrument.

4. Data Processing

[33] To minimize the influence of the wavelength shift due to instrument temperature, only observations with the first band situated between 1.0175 μm and 1.0255 μm are processed. A uniform −7.5 nm shift is applied to the wavelengths table in the VIRTIS data cubes to better reconcile data with synthetic spectra. Parameters empirically derived during processing either have the subscript b, giving band number as integer starting at zero, or λ giving band position in micrometer. The first pertains to all images of that band regardless of individual band positions while λ denotes that the parameter in question is seen as a function of individual band position wavelength of individual observations.

[34] Several different VIRTIS bands are situated inside the window regions. The band with the best ratio of surface to atmospheric influence is $b = 0$, on average at $\lambda = 1.021$ μm. The band closest to the center of the 1.31 μm is at $b = 30$ on average at $\lambda = 1.307$ μm. Analysis of VIRTIS data is performed only for band 0 for the surface signal and band 30 for the cloud signal, although the data processing mechanism may as well be extended to other windows and bands farther from the center (e.g., Figure 4). It is possible to use the average of several or all bands showing a signal from the surface with this approach. This would increase SNR for individual observations and help in the detection of transient temperature variations, e.g., thermal signature of active volcanism. The contrast related to surface emissivity, however, is decreased in the averaged image as the transparency of the atmosphere is greatest in the small wavelength range used here.

[35] Only observations with 3.3 s exposure duration or greater have a sufficient SNR ratio. In total 1161 case 2 and 3 observations have been selected for processing. Observations span a period from May 2006 to December 2007. Some observations contain frames, where all spectra of one line are offset relative to the neighboring frames. These frames are not processed and appear as horizontal lines of missing data in VIRTIS images (Figure 9).

4.1. Scattered Sunlight

[36] VIRTIS image cubes on the nightside are affected to some extend by sunlight. While sunlight scattered by the upper atmosphere extends to at least 95° of incidence, the bright illuminated crescent of Venus close to the field of view of VIRTIS also causes stray light within the instrument. The same is true for direct sunlight, which is however, due to the geometry of the orbit, less relevant for the case 2 and 3 observations than for case 1 [*Arnold et al.*, 2008]. *Meadows and Crisp* [1996] use a spectrum extracted from the sunlight crescent as template for the removal of stray light from the 1 μm region. The spectrum is scaled to fit the radiance at the 1.4 μm CO_2 absorption band for each of their spectra and then subtracted.

[37] In a similar approach here the spectral average of the VIRTIS bands 36 to 39 is used as parameter $\overline{I_{[36,39]}}$ for the spatial distribution of stray light. To determine the spectrum of stray light, a linear regression is performed over all VIRTIS observations for the radiances of VIRTIS bands 0 to 35 against this parameter assuming a direct proportionality between the stray light seen at $\overline{I_{[36,39]}}$ and the radiance of other bands I_b. The linear regression retrieves the best fitting parameters a to the equation

$$I_b = V_b + S_b \overline{I_{[36,39]}} \tag{5}$$

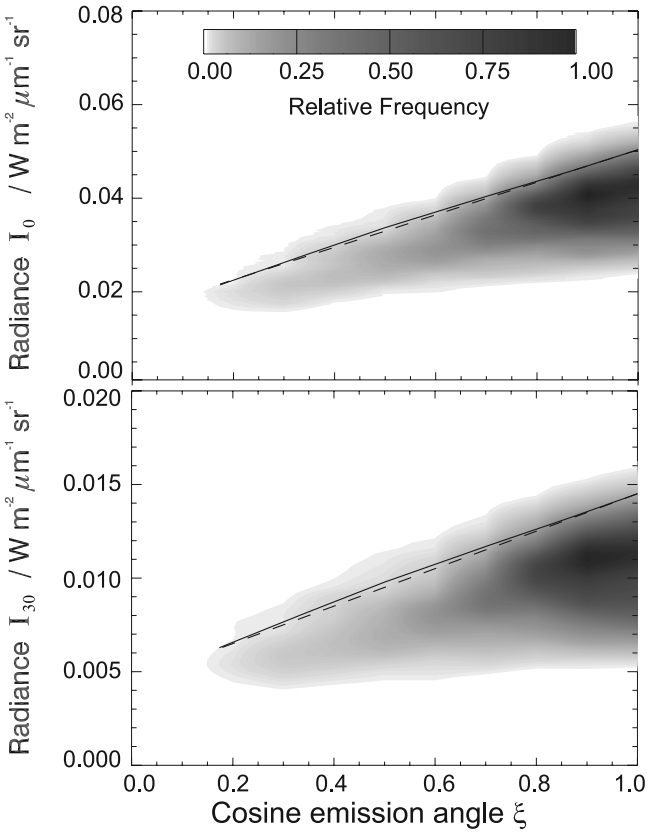

Figure 5. Distribution of surface window radiance I_0, atmospheric window radiance I_{30}, and corresponding cosines of emission angles ξ; only data points with negligible stray light $\overline{I_{[36,39]}} \leq 0.005$ W m^{-2}sr^{-1} μm^{-1} are considered. Frequency distribution is scaled to yield one at maximum. Solid line is created from synthetic spectra of the nightside at different emission angles, and dashed lines are function $P(\xi) = 0.31 + 0.69\xi$ scaled to fit synthetic spectra at nadir.

This separates the flux I_b spectra into two terms, first thermal emission of Venus V_b which is not correlated to flux at bands 36 to 39 but represents average thermal emission, and second stray light spectrum S_b as the coefficients of proportionality of I_b to $I_{[36,39]}$. The linear relation extends to a value of approximately $I_{[36,39]} = 0.01$ W m$^{-2}\mu$m^{-1}sr^{-1} and only points in this range are used for the regression and further processing.

[38] Comparison of VIRTIS spectra with the stray light spectrum S_b scaled to fit radiance at bands 36 to 39 demonstrates that there is a good fit at absorption bands while at window wavelengths, stray light is slightly increased above the lower envelope of the VIRTIS data spectrum, see Figure 4. Individually scaled stray light spectra are subtracted from each data spectrum to isolate the local flux of thermal emission:

$$I'_b = I_b - S_b\overline{I_{[36,39]}} \tag{6}$$

The values relevant for data processed here are $S_0 = 3.30$ and $S_{30} = 1.32$.

4.2. Limb Darkening

[39] Limb darkening due to scattering in the upper clouds affects all VIRTIS images, most severely in off-nadir case 2 and in case 3 southern hemisphere mosaics. The limb darkening of synthetic spectra agrees well with VIRTIS radiances (Figure 5) and shows that the angular distribution of emitted radiance I'_b does not significantly vary between the 1.02 μm and the 1.31 μm window. The angular distribution of radiance with respect to cosine of emission angle ξ can be described as product of nadir radiance $I'_b(1)$ and limb darkening function $P(\xi)$.

$$I'_b(\xi) = I'_b(1)P(\xi) \tag{7}$$

Required for the two stream approximation employed here is hemispherically integrated flux [*Goody and Yung*, 1989]

$$\begin{aligned} F_b &= 2\pi \int_0^1 I'_b(\xi)\xi d\xi \\ &= 2\pi I'_b(1) \int_0^1 P(\xi)\xi d\xi \end{aligned} \tag{8}$$

To account for viewing angles, the radiance $I'_b(\xi)$ measured at each pixel is divided by the limb darkening function $P(\xi)$ determined by interpolation of synthetic spectra at different emission angles scaled to unity at nadir ($\xi = 1$), see solid line in Figure 5. The angular integration is performed by approximating $P(\xi) = 0.31 + 0.69\xi$ which in conclusion yields

$$F_b = \pi 0.77 \frac{I'_b(\xi)}{P(\xi)} \tag{9}$$

4.3. Projection and Smoothing of Magellan Altimetry

[40] The Magellan global topography data record (GTDR) from the planetary data system (PDS) gives topography of the surface of Venus [*Ford and Pettengill*, 1992]. For the VIRTIS observations, the data are projected on the VIRTIS field of view and incorporated in the ancillary geometry data files distributed together with VIRTIS hyperspectral cubes. Since the thermal emission of the lower atmosphere and surface is scattered in the clouds, the radiance observed by VIRTIS originates in the cloud layer illuminated by the surface and atmosphere below. This has two consequences: First, the altitude relevant to a pixel is not given by the intercept of the line of sight (LOS) with the surface, but by the altitude directly below the intercept of the LOS with the cloud layer. Second, not only the point directly below LOS cloud intercept but the neighboring area contributes to illumination of the clouds at this point. This results in a smearing of the image of the surface. Simulations by *Hashimoto and Imamura* [2001] describe this effect as photons from a point source on the surface scattered into a gaussian distribution with full wide half maximum (FWHM) of 90 km above cloud level. *Moroz* [2002] approximates a spatial resolution of 100 to 200 km.

[41] To simulate this effect, the Magellan altimetry in the VIRTIS geometry is projected according to VIRTIS image viewing geometry to a height of 65 km corresponding to the upper main cloud deck. The spatial resolution of VIRTIS images varies on the southern hemisphere between approx-

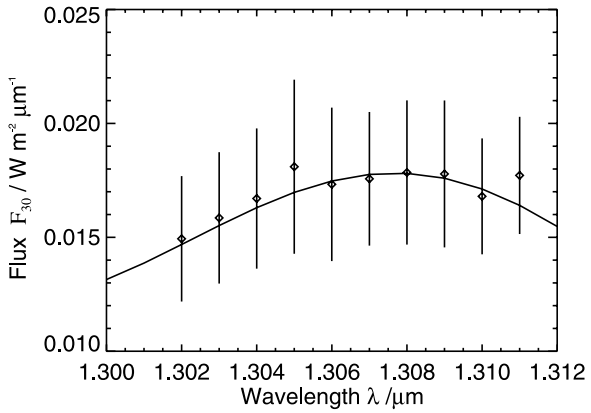

Figure 6. VIRTIS fluxes F_{30} binned according to band position λ with 1σ uncertainty. Solid line is synthetic flux spectrum from plot 1 reduced in spectral resolution by convolution with a gaussian with full wide half maximum (FWHM) of 18 nm and scaled with a factor of 1.36. Assuming cloud transmittance of 0.18 [*Hashimoto and Sugita*, 2003], this spectrum is used for approximation of spectral dependance of T_{30}.

imately 10 and 60 km. The spatial resolution of the projected altimetry has to be aligned with the spatial resolution of the thermal emission flux penetrating the atmosphere. To achieve this task, a moving weighted average is applied. The weighting function is a gaussian with respect to distance from pixel center on the surface and has a FWHM of 100 km. There are some complications to the problem of connecting thermal emission flux and altimetry.

[42] First, flux is calculated by angular integration of the blackbody radiation. The hemispherical integration through the factor of π is only exact for plane surfaces, here no attempt has been made to account for curvature of the topography. Second and more important, thermal emission radiance is not linear to surface altitude. Because thermal emission varies strongly with temperature, low altimetry areas contribute unproportionately more to the brightness of a region than higher areas in the same region. On the other side atmospheric transmittance at highland regions is higher. Averaging over altimetry instead of thermal flux leads to an error depending on distribution of altimetry values within the smoothing radius; it is most severe in regions with high slopes and altitude differences.

[43] To minimize this error without detailed simulations of radiative transfer, the smoothing algorithm is used in two different ways. For the determination of global atmosphere and surface parameters (section 4.4), the moving average is applied directly to altimetry. Thus, smoothed Magellan altimetry is denoted by Z in units of meters relative to mean planetary radius (MPR) of 6051.84 km [*Ford and Pettengill*, 1992]. For the calculation of local flux anomaly (section 4.5), the thermal emission flux is calculated on the basis of global brightness temperature to altimetry relation 8 and the original Magellan altimetry projected on the VIRTIS field of view. The moving average is then applied to the thermal flux.

[44] The difference between flux calculated from the smoothed altimetry, and the smoothed flux is on average 0.04%. In some regions, especially rifts, the difference is higher but does not exceed 2%. No strong dependance of the difference to surface altitude has been found, the error in the determination of global brightness temperature is assumed to be small. The width of the smoothing weighting function is likely a more critical parameter but no study of its influence has been made yet.

4.4. Atmospheric Parameter Determination

[45] Equation (3) relates emerging flux at surface window to three parameters: r, a_λ, and $T_\lambda(Z)$. Typical cloud reflectance of $r = 0.82$ based on a nominal cloud model is given by *Hashimoto and Imamura* [2001]. Adopting this value in equation (2) and assuming of $F_\lambda^{\mathrm{therm}} = 0.77\pi B_\lambda[T_\lambda]$ leads to a temperature of the atmosphere below the clouds T_λ. Shape of the synthetic spectrum (Figure 1) is used to fit spectral dependance of T_λ to average VIRTIS flux at different wavelengths (Figure 6). The resulting range of T_{30} from 528 K to 531 K approximately corresponds to VIRA atmospheric temperature at 26 km height for all wavelengths covered by band 30. Flux F_{30} measured with VIRTIS band 30 and estimated T_{30} allow to calculate local cloud reflectivity r with equation (2).

[46] The two remaining parameters are estimated from VIRTIS and Magellan altimetry data. While atmospheric temperature at the mean planetary radius of 735 K and surface emissivity $\varepsilon_0 > 0.8$ are relatively well constrained by in situ measurements, adopting these values as $\varepsilon_0 = 1 - a_0$ and $T_0(0\ \mathrm{km}) = 735$ K does not work well because lowest atmosphere scattering and absorption is not accounted for. Albedo a_0 is expected to be greater than 0.15, which *Meadows and Crisp* [1996] used to represent the basaltic plains of the surface. Temperature T_0 with respect to equation (3) will be less than real surface temperature since the lowest atmosphere is not fully transparent.

[47] To estimate a_0, the distribution data points in the F_0, F_{30}, and Z space is determined using all VIRTIS observations. Average value of F_0 in each F_{30} interval is given with 0.5σ error bars for different topography intervals in Figure 7. The position on the F_{30} axis translates with equation (2) into cloud reflectivity r. Figure 7 demonstrates that it is possible to reproduce the relation of observed fluxes F_0 and F_{30} within 0.5σ with a lowest atmosphere and surface albedo $a_0 = 0.22$ independent from topography and temperature $T_0(Z)$ as monotonic function of altitude. Variation of a_0 with band position λ has not been investigated. Preliminary analysis of the windows at 1.10 and 1.18 μm not presented here yields similar values of lowest atmosphere albedos, which leads to the conclusion that this parameter does not vary strongly with wavelength.

[48] Using this constant, a_0, equation (3) is solved for T_0 for each data point. Next, the distribution of T_0 values in the topography Z and band position λ space is determined from all processed data points. A two dimensional polynomial of degree 2 with coefficients k_{nm} and parameters Z and λ is fitted to the averages of T_0 to obtain an analytical approximation of $T_\lambda(Z)$:

$$T_\lambda(Z) = \sum_{i,j=0,0}^{2,2} k_{ij} Z^i \lambda^i \tag{10}$$

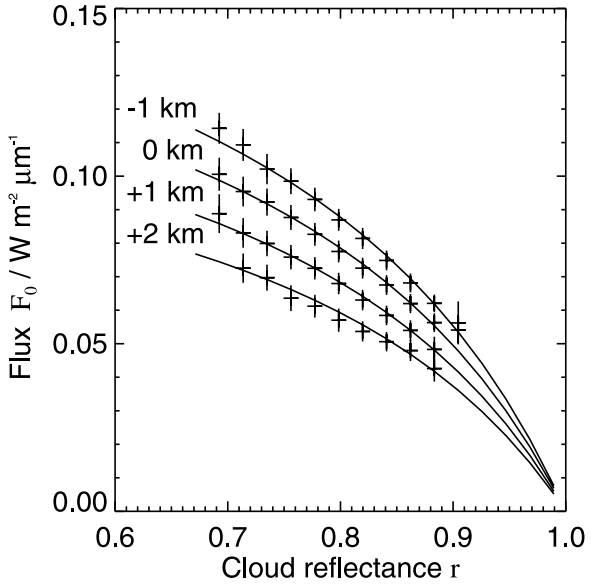

Figure 7. Average of surface window flux for different altitudes as a function of cloud reflectivity r. Flux uncertainty is given as 0.5σ. Size of topography bins is 500 m. Curves are calculated with equation (3) with a_0 = 0.22 for all heights and $T_0(-1\text{ km}) = 712$ K, $T_0(0\text{ km}) = 708$ K, $T_0(1\text{ km}) = 703$ K, and $T_0(2\text{ km}) = 698$ K. Figure 7 shows that equation (3) describes the relation between surface and atmosphere window flux well and thus can be used for removal of cloud contrast.

The $i \times j$ matrix of coefficients is

$$k_{ij} = \begin{pmatrix} 63.6 \times 10^3 & -12.3 \times 10^3 & 60.3 \times 10^3 \\ 13.0 & -25.6 & 12.5 \\ -1.83 \times 10^{-3} & 3.62 \times 10^{-3} & -1.79 \times 10^{-3} \end{pmatrix} \quad (11)$$

Units of k_{ij} are $\text{m}^{-j}\mu\text{m}^{-i}$ K where i is index of column and j is index of row starting with zero.

[49] The Z-λ isolines determined directly from the data and from the fit of equations (10) and (11) are illustrated in Figure 8 for seven temperatures. The lapse rate of -4 to -5 K km^{-1} is not consistent with the -8.06 K km^{-1} in the VIRA model but this is not surprising since scattering, absorption and emission in the atmosphere lowers the lapse rate of observed flux. Furthermore scattering and absorption optical path from surface to top of atmosphere is determined by topography. Usually this is negligible, as topography is only a fraction of total optical path lengths, but extinction is here strongly concentrated toward the lowest part of the atmosphere owing to Rayleigh scattering being proportional to density and the continuum absorption being proportional to square of density [*Pollack et al.*, 1993].

4.5. Image Processing

[50] After the parameters necessary for atmospheric correction are either assumed or determined from the statistical behavior of VIRTIS data points, the next step is the application of equation (3) on each observation to analyze the local thermal flux. Data pixels are processed only when the following conditions are met: (1) emission angle is less than 80°, (2) incidence angle is greater than 95°, and (3) sunlight parameter $\overline{I_{[36,39]}}$ is less than 0.01 W $\text{m}^{-2}\mu\text{m}^{-1}\text{sr}^{-1}$.

[51] Two different quantities are retrieved, either surface temperature T_0 or the thermal flux anomaly A_0 which is thermal emission corrected for the global relation of surface temperature $T_\lambda(Z)$ to altimetry and band position. Figure 9 illustrates the process of retrieving surface and lowest atmosphere brightness temperature. Both results are map projected for each observation using Lambert's azimuthal equal area projection centered on the south pole. The projected individual images are then combined by using the median of all different observations of the same place. The spatial distribution of processed images is shown in Figure 10.

5. Results

[52] Surface temperature parameter T_0 averaged over time is highly correlated with altimetry in Figure 11. Signal to noise is better in the hemisphere west of 0° longitude as is expected owing to greater coverage (Figure 10). SNR generally decreases toward the limb, where less images as well as less spectra per unit area have been acquired owing to the generally oblique viewing angles. The polar region is usually seen at low emission angles but stray sunlight increases the error although spectra surpassing a certain threshold of stray light are discarded during processing.

[53] The map of flux anomaly Figure 12 presents in principle the same data as Figure 11 but corrected for the global temperature to topography relation (Figure 8). There are however some correlations with topography remaining when comparing the altimetry contours in Figure 11 with flux anomaly in Figure 12. There is lower flux in the sector between $-120°$ and $-110°$ longitude starting at about 75° to 60°S latitude and extending at least to the equator. This coincides with an increased uncertainty in the Magellan altimetry investigated by *Rappaport et al.* [1999]. Several rifts, e.g., Artemis Chasma in V-48, show contrast in the flux anomaly map. This might be related to the difficulties in smoothing of the radar altimetry (section 4.3). The error

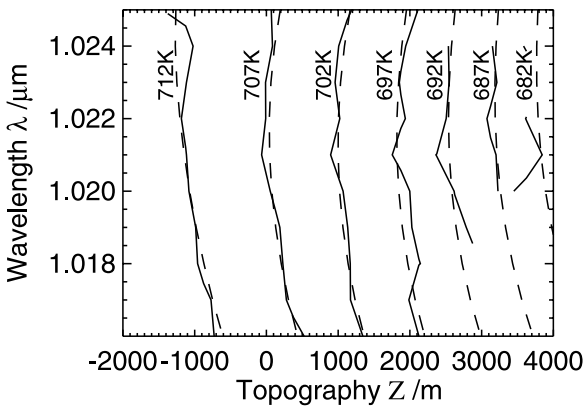

Figure 8. Relation of lower atmosphere surface brightness temperature T_0 (for seven different values of T_0) to topography Z and band position λ. Solid lines are isolines of average data temperature. Dashed lines are polynomial fit to data.

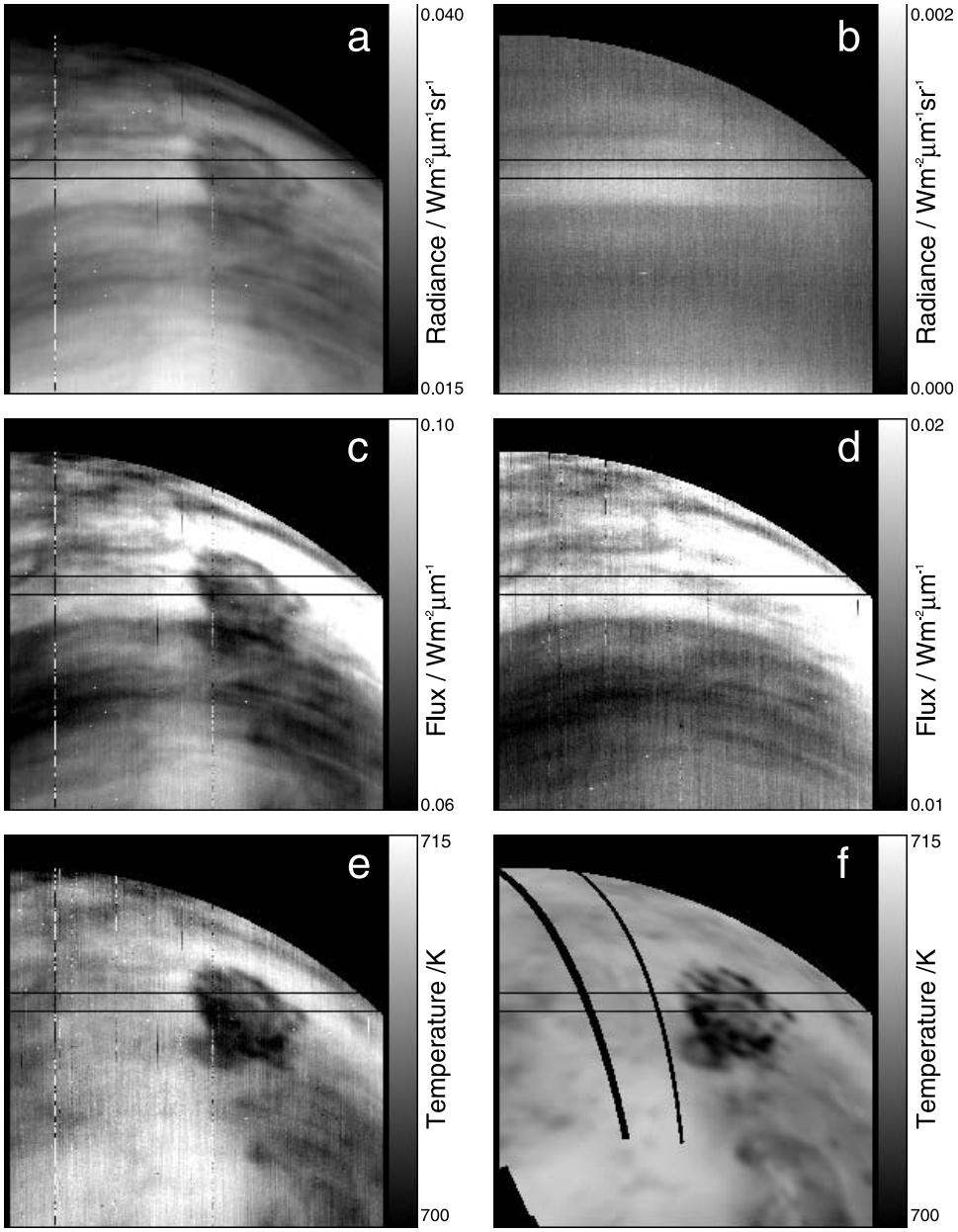

Figure 9. VIRTIS image VI0373_01 (second image acquired in orbit 373) during several processing steps: (a) band 0 at 1.02405 μm; (b) spectral median of bands 36 to 39 showing distributions of stray light; (c) band 0 corrected for stray light and limb darkening; (d) band 30 corrected for stray light and limb darkening; (e) brightness temperature of lower atmosphere and surface derived from band 0 and band 30; and (f) surface temperature map constructed from Magellan altimetry and $T_\lambda(Z)$. Horizontal dark lines are data points not processed owing to an offset of the whole frame.

due to the smoothing is expected to be greatest in regions with steep slopes and large altitude differences.

[54] The equatorial regions generally show a greater residual correlation of flux and topography. This might be indicative of a latitudinal component in the flux to topography relation, which might be due to latitudinal temperature or atmospheric composition variation. Most data points used for determination of the global flux to topography relation are in the midlatitude to low-latitude regions between 25° and 75°S where influence of topography seems to be well accounted for (compare Figure 10 and Figure 12). Spectrometer temperature and thus band position λ varies with orbital position. The equatorial regions have a bias to be observed at wavelengths displaced from the optimum. Determination of $T_\lambda(Z)$ is therefore possibly less reliable for the equatorial regions. The lower latitudes are, with some exceptions that are described in sections 5.1–5.3, very well represented by the global flux to topography relations as the flux anomaly is very near to zero.

5.1. In Situ Sites

[55] There are four in situ measurements of surface rock composition on the southern hemisphere, see Figure 12. The Venera 8 landing site in quadrangle V-43 is in a region with

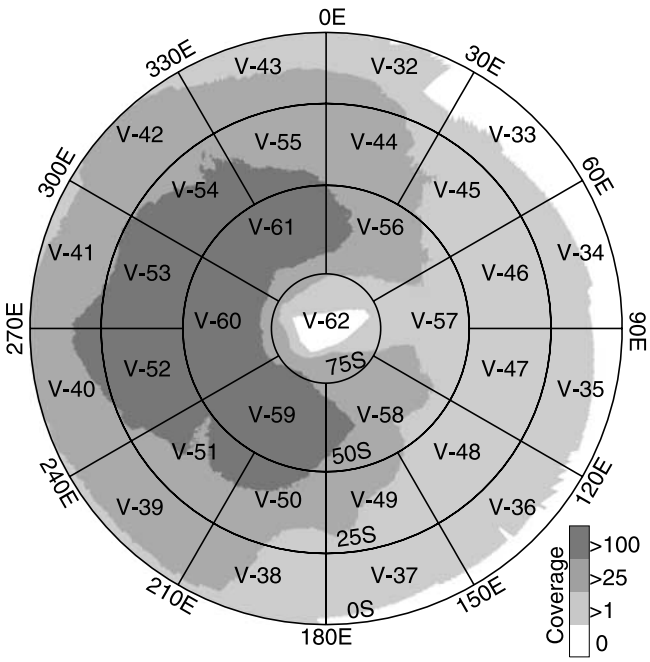

Figure 10. Spatial distribution of processed images in Lamberts azimuthal equal area projection centered on the south pole and extended to the equator; labels denote Venus mapping quadrangles.

average to low thermal flux. Venera 13 in quadrangle V-42 is in the region with low flux adjacent to Doliya tessera, Venera 14 is on the gradual transition from this same diffuse low flux area to the diffuse high flux area over Navka planitia. Vega 2 landed on Rusalka planitia in quadrangle V-37 which shows an unreliably determined flux. All landing sites are in the equatorial regions and not very well covered by VIRTIS observations. Possible interpretations of rock types are summarized on the basis of the work of *Kargel et al.* [1993]. Venera 8 measured abundances of natural radioactive isotopes of K, U, and Th, which where consistent with several terrestrial analogues, including rhyolite (volcanic rock of felsic composition), monzonite (intermediary composition) and leucitite, an on Earth rare alkaline mafic volcanic rock in which felsic minerals are mostly replaced by the feldspathoid mineral leucite. Leucitite is also proposed for the Venera 13 landing site, where elemental abundances were more directly measured by X-ray fluorescence spectroscopy. The Venera 14 and Vega 2 samples also analyzed with XRF spectroscopy are interpreted to have basaltic composition similar to mid-ocean ridge basalts. Though it might be tempting to attribute areas of low flux anomaly to the exceptional samples of Venera 8 and Venera 13 situated in the vicinity, very little difference is seen in NIR flux anomaly between the Venera 8, Venera 13, and Venera 14 sites.

5.2. Relation to Geological Settings

[56] The thermal flux anomaly shows some correlation with geomorphological terrain types and also individual features. Over large areas of tessera terrain the flux adjusted for topography is generally lower than in neighboring areas. The tessera terrain outlines in Figure 12 are taken from the electronic global geological map accompanying the work of *Tanaka et al.* [1997]. Large tessera terrains with relative good SNR are Phoebe regio and Doliya tessera in V-41, Alpha regio in (among others) V-32, Lhamo and Cocomama tessera in V-56. Tessera boundaries are however not well defined in NIR flux, negative flux anomalies are interspersed with average flux and occasional positive anomalies. For instance, at Doliya tessera no relation of its boundaries to flux is obvious, but instead the tessera area is situated directly on the boundary between larger areas of positive and negative flux anomalies.

[57] The negative flux anomaly over tessera regions is consistent with the relative low surface emissivity at highlands retrieved by *Hashimoto et al.* [2008] from the Galileo NIMS flyby data. Tessera are more frequent in highlands [*Ivanov and Head*, 1996]. Their approach does not correct for topography empirically but uses a flux to topography relation derived from the adiabatic lapse rate and radiative transfer modeling and is therefore not directly comparable to this result.

[58] Tessera are not extensively covered by VIRTIS observations; there is very little data yet of the large tessera highlands in Aphrodite terra. Most VIRTIS spectra were acquired on midlatitudes to low latitudes <25°S between 180° and 360°E longitude, dominated by tectonically modified lowland plains. Highlands in this area are Imdr, Ishkus, Thetis, and Dione regios where some, but not all, large volcanic edifices show a flux exceeding average flux at comparable altitude by 5%, listed in Table 1. Two coronae are also listed. The area of these flux anomalies is significantly smaller than the topographic rise and concentrated on the flank.

[59] A similar but larger anomaly is found at the southern flank of the Quetzalpetlatl corona rise in Lada terra, 0°E 70°S. The southern boundary of this anomaly is not clearly defined as it borders on the polar area with small SNR ratio. The fan shape nevertheless correlates with the large lava flows Juturna and Cavilaca fluctus, extending from the rim of Boala corona, nested inside Quetzalpetlatl corona. For most recent radar imaging see the work by *Kratter et al.* [2007]. The contours of digitate plains units from the electronic material accompanying *Tanaka et al.* [1997] are outlined in Figure 13. *Ivanov and Head* [2006] characterized the unit containing the positive flux anomaly south of Quetzalpetlatl as tectonically undeformed lobate plains. Lavinia planitia in V-55 shows an overall increased flux compared to other planitia regions at altitudes below mean planetary radius and especially prominent at the eastern basin rim. This basin rim is characterized by several lobate lava flows and plains (Figure 13), emanating from coronae, volcanoes or the Lada rift [*Magee and Head*, 1995]. These units are designed stratigraphically young, undeformed lobate plains in the map by *Ivanov and Head* [2001]. The spatial correlation is, however, less significant than at the lava streams south of Quetzalpetlatl and the anomaly does not exceed 10%. For a more detailed analysis of the NIR flux anomaly at Quetzalpetlatl see *Helbert et al.* [2008].

5.3. High-Altitude Radiothermal Anomaly

[60] Radiothermal emissivity as measure by the Magellan mission [*Pettengill et al.*, 1992] distinctly drops off from a value around 0.85 to a value of 0.4 above surface elevations

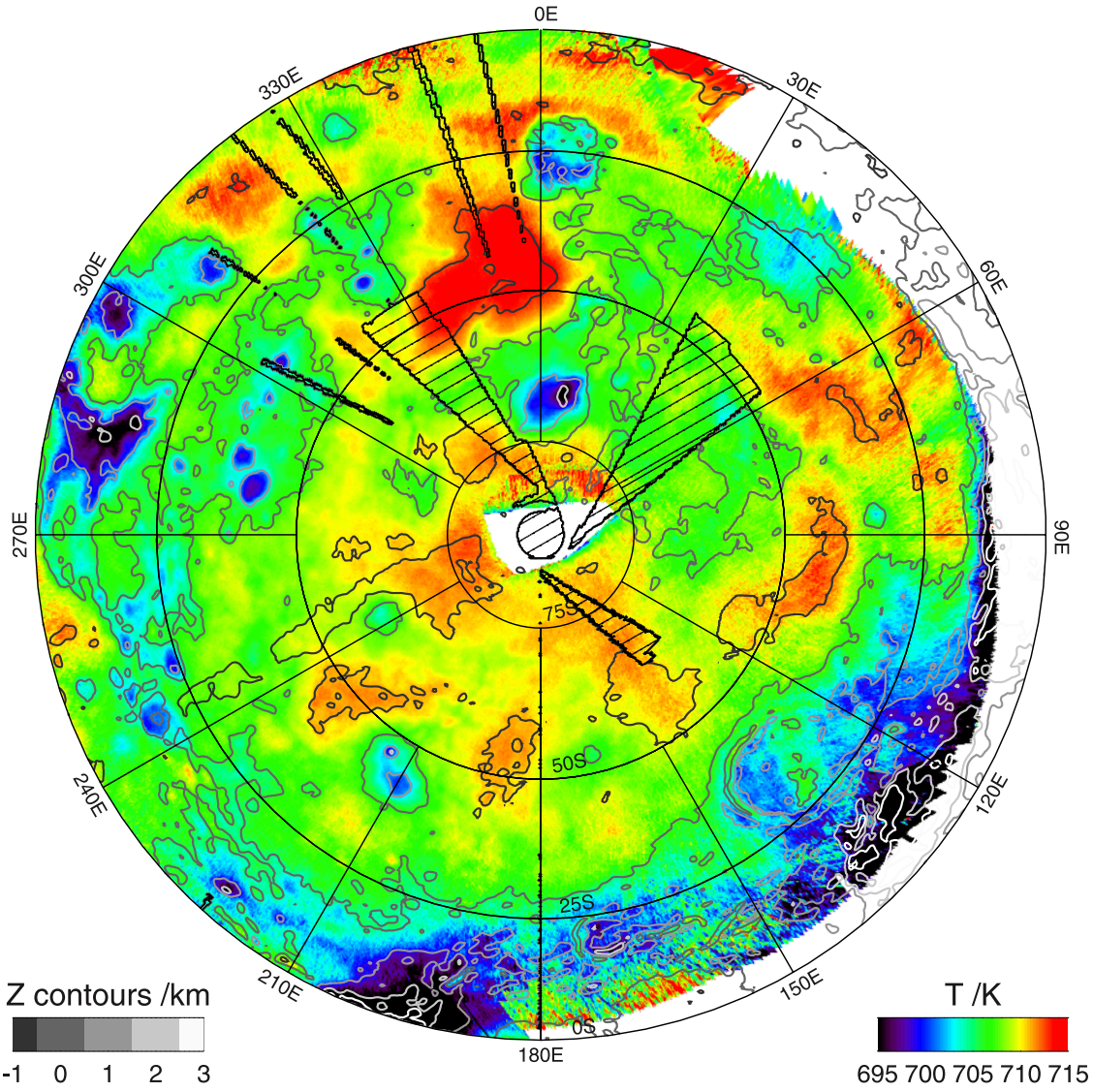

Figure 11. Surface lower atmosphere brightness temperature T_0 mosaics in Lamberts azimuthal equal area projection centered on the south pole. Magellan altimetry is plotted with 1 km contours. Black hachures denote missing altimetry data. Temperature is well correlated with altimetry, although influence of wavelength shift is not equal in all regions.

of 4 to 5 km [*Wood*, 1997]. This height is rarely reached in the area mapped by VIRTIS with good SNR. Areas with radiothermal emissivity less than 0.7 are marked on the flux anomaly map in Figure 12 by dark hachures from up left to down right. A single region with a radiothermal emissivity anomaly, quadrangle V-41, Yunya-mana mons (285°E, 18°S) is mapped with reasonable SNR and shows no significant flux anomaly in NIR. However, the extent of this area is close to spatial resolution of the NIR data and observed flux might be influenced by the neighboring tessera terrain. The Venus Monitoring Camera (VMC) also on Venus Express did not observe resolvable emissivity variations in this region (Basilevsky et al., submitted manuscript, 2008).

[61] Repeated coverage of large regions showing a radiothermal emissivity, e.g., Thetis regio in V-36, is required to analyze the radiothermal anomaly in NIR. The approach used here is however not very well suited for this investigation. The influence of any present altitude-dependent variation of emissivity will be to some extent removed during the processing owing to the empirical determination of $T_\lambda(Z)$. A nonempirical approach that correctly accounts for absorption and scattering independent from VIRTIS data in the lowest atmosphere, as in the work of *Hashimoto et al.* [2008] or *Arnold et al.* [2008], is required. Data at higher latitudes and altitudes, e.g., Maxwell Montes are also desirable, but will not be available in observations other than case 1 northern hemisphere sparse imaging.

6. Discussion

[62] Interpretation of the thermal flux anomaly is highly ambiguous. First, a flux anomaly due to surface emissivity cannot be distinguished from surface temperature effects with this approach. The long period of one and one half year over which the data are averaged and the properties of the

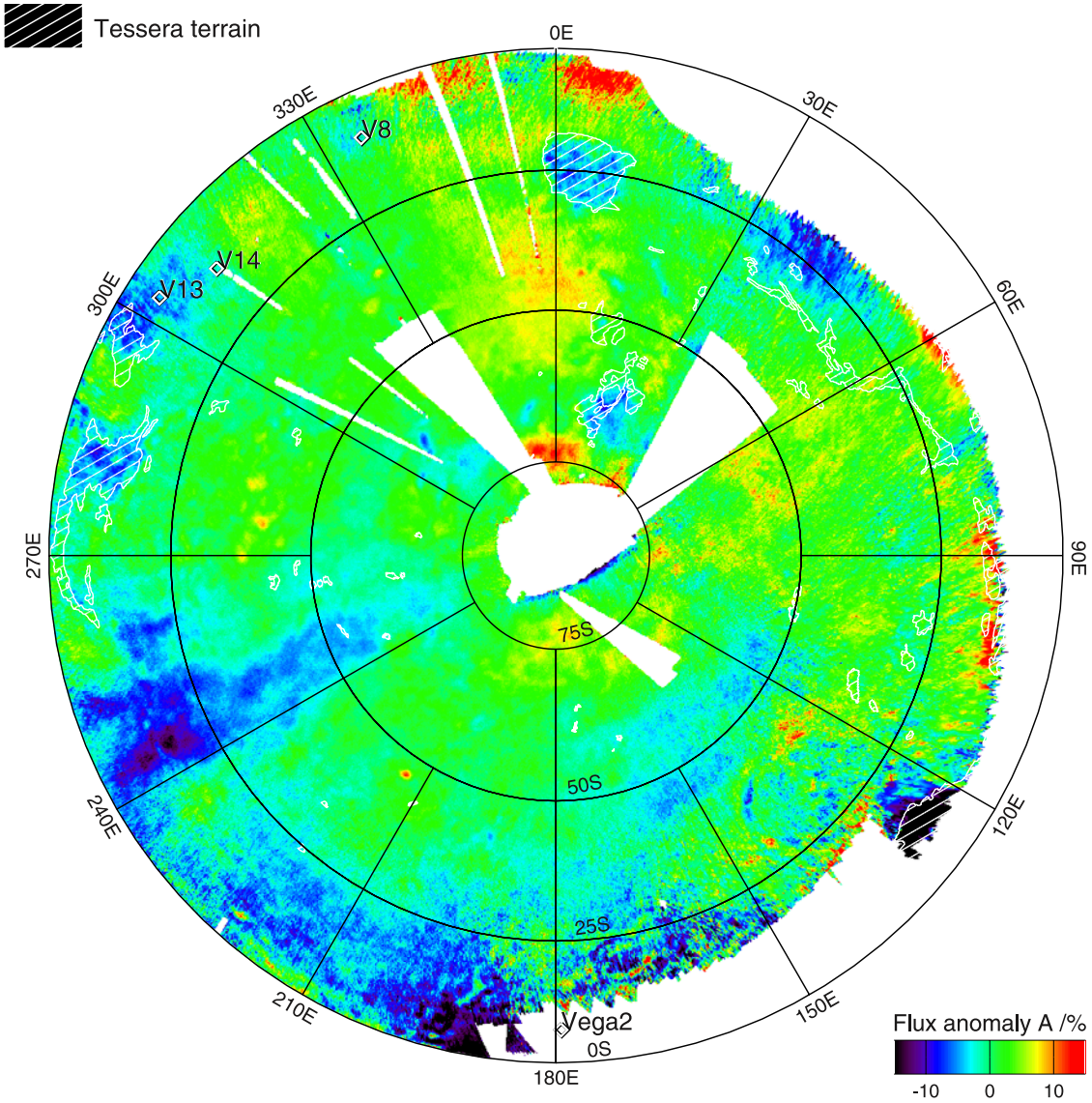

Figure 12. Map showing flux anomaly A_0 in relation to in situ measurements and tessera terrain. Landing site coordinates of Venera and Vega probes are from *Basilevsky and Head* [2003]. Tessera terrain outlines are from the electronic material accompanying the article by *Tanaka et al.* [1997]. Relation to in situ measurements is inconclusive. Tessera show a negative flux anomaly. Flux over tessera terrain is less than in plains and volcanic rises of the same Magellan altimetry values. Only areas with a coverage of three or more VIRTIS images are mapped here.

lower atmosphere of Venus (see section 2.1) preclude, to first approximation, local surface temperature variation due to atmospheric or insolation effects. Endogeneous heat, e.g., active volcanic vents or even lava flows, could also be a source of thermal NIR flux and the coincidence of positive flux anomalies and relatively young volcanic features presents this as an attractive explanation. However, the recent rate of extrusive volcanism is comparable to intraplate volcanism on Earth [see *Grimm and Hess*, 1997, and references therein]. Cooling heat flux of liquid lava on the surface is slightly lower than on Earth [*Snyder*, 2002], but cooling time scale of the lava is estimated to be in the order of 1 day; that is, an eruption is not detectable for more than 1 day after its end [*Hashimoto and Imamura*, 2001]. Areas of increased flux are up to the order of hundreds of

Table 1. Volcanic Edifices Correlated With Positive Flux Anomaly[a]

Name	Coordinates	Diameter (km)	
		Anomaly	Structure
Mertseger mons	270°E, 37°S	125	450
Shiwanokia corona	278°E, 42°S	200	500
Shulamite corona	284°E, 39°S	200	275
Idunn mons	215°E, 46°S	150	250
Hathor mons	324°E, 38°S	250	333
Ininni mons	328°E, 34°S	125	339

[a]Names, coordinates, and diameters of volcanic edifices are from the Web page of the USGS Astrogeology nomenclature database (available at http://planetarynames.wr.usgs.gov/). Two coronae are included in this compilation; their flux anomaly is located on the flank of the topographic rise but outside the annulus.

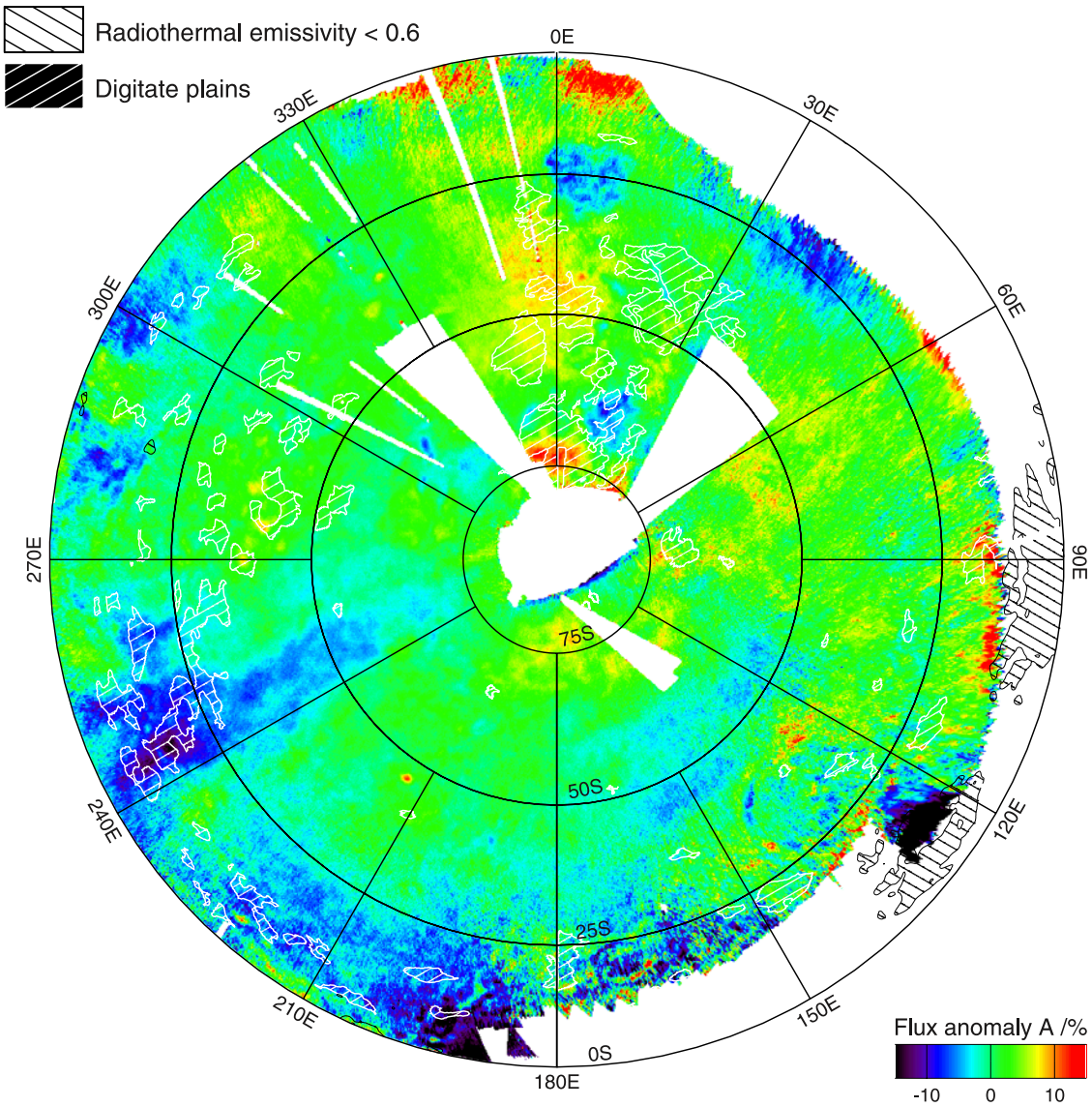

Figure 13. Map showing flux anomaly A_0 in relation to plains with a flow-like morphology and to the radiothermal emissivity anomaly in high regions. Digitate plains outlines from the material accompanying *Tanaka et al.* [1997]. Correlation of radiothermal end NIR emissivity is inconclusive owing to the insufficient coverage and the nature of the topographic correction. Most prominent coincidence of positive flux anomaly and digitate plains is on the southern flank of Quetzalpetlatl corona, 0°E and 70°S. This plains unit is composed of the large lava flow fields fan shaped extending from Boala corona on top of the topographic rise [*Ivanov and Head*, 2006].

thousands of square kilometers, temporal sampling rate is at most one or two images per day, typically much less. The map is a temporal median of up to several tens of images, and therefore filters the effects of short or even singular events with significantly increased temperatures. All individual observations (i.e., the result presented in Figure 9) have been searched for clear evidence of an active volcanic eruption but none has been found yet. Volcanic vent activity can be continuous but is also difficult to reconcile with the extend of the flux anomaly. Owing to these considerations, here flux anomaly is interpreted in terms of surface emissivity.

[63] Second, interpretative ambiguity is that variation of surface emissivity known at only one wavelength is difficult to assign to a certain surface material. As only one point in the surface spectrum is spatially mapped, the emissivity is interpreted as a result of relative ratio of felsic to mafic mineral abundances. Felsic minerals (i.e., feldspars and quartz) generally have a low emissivity at 1 μm while mafic (Mg- and Fe-rich) minerals tend to high emissivities, which would allow to distinguish between felsic granite and mafic basalt [*Hashimoto and Sugita*, 2003]. The poorly known chemical weathering environment complicates the interpretation of surface emissivity with respect to composition of terrestrial analogues. Minerals affecting emissivity such as pyrite or magnetite might be unstable depending on surface temperature and atmospheric redox state [*Fegley et al.*, 1997; *Hashimoto and Abe*, 2005]. *Wood* [1997] relates the high-altitude radiothermal emissivity anomaly to volatile

transport of magnetite from the hot lowlands to the mountaintops. This would affect NIR emissivity as well but no evidence has been found by *Lecacheux et al.* [1993], *Meadows and Crisp* [1996] or Basilevsky et al. (submitted manuscript, 2008). Owing to the empirical nature of this approach, it is very difficult to investigate any present altitude-dependent emissivity trend, though a comparison of VIRTIS data of comparable high altitudes with and without radiothermal anomaly would be very interesting but difficult owing to the orbit of Venus Express.

[64] Weathering age might affect surface emissivity independently from altitude. If emissivity constantly decreases with time, e.g., by slow and steady volatile transport of magnetite from the lowlands to the highlands above 4 km height [*Wood*, 1997], the observed thermal flux anomaly will denote differences in surface age. Increased thermal flux is more frequently found at tectonically undeformed and probably younger areas as opposed to the lower flux over the stratigraphically old and deformed tessera. However, the small thickness of material contributing to NIR surface emissivity dictates that the weathering effects in emissivity take place relatively rapid and then reach an equilibrium state. The large areas with increased emissivity would require that weathering time scale is not small against volcanic resurfacing time scale. From a very general and preliminary view on stratigraphic age, a weathering process that lowers emissivity over time scales of the average age of the surface of about 0.5 Ga is consistent with observed flux anomalies. Weathering should not be disregarded as possible explanation for the flux anomalies. Further hypotheses, as to which kind of surface material regardless of any weathering effects might be responsible for observed flux anomalies, are presented in sections 6.1 and 6.2, and their plausibility is discussed.

6.1. Relative Felsic Composition of Tessera Terrains

[65] In the plains, a basaltic composition is supported by the low viscosity inferred from radar images and in situ measurements. No direct morphological evidence for composition and no in situ measurement exists for tessera terrain, which is characterized by complex tectonic deformation patterns. The crater frequency of tessera terrain is not distinctly different from that of plains, but this does not necessarily imply same age since tessera terrain might have undergone tectonic deformation that reset the crater history. At most boundaries tessera terrain is embayed by neighboring plains and therefore stratigraphically older as well as elevated in topography when visible. It more frequently occurs at higher surface altitudes [*Ivanov and Head*, 1996]. Several plateau shaped highland regions are composed mostly of tessera terrain. These highlands generally show a small geoid to topography ratio which implies shallow depth of compensation due to either density or thickness variations of the crust [*Smrekar and Phillips*, 1991].

[66] On the basis of these properties, tessera may represent the granitic cratons that *Taylor and Campbell* [1983] hypothesized to exist on Venus. If tessera terrain were indeed the venusian analogue to archean continental nuclei on Earth the implications would be far-reaching. Under current dry surface conditions and stagnant lid tectonic regime creation of silicic (i.e., granitic) magmas is unlikely since subduction of water rich crust is required [*Taylor and Campbell*, 1983]. D/H ratio measured in the atmosphere of Venus is consistent with evaporation of a primordial ocean of several tens of meters deep and subsequent preferential loss of hydrogen by atmospheric erosion [*Donahue and Russell*, 1997]. Under cooler and wetter conditions the accordingly different temperature and rheological contrasts in the mantle and crust might have resulted in continuous plate tectonics [*Solomatov and Moresi*, 1996; *Stein et al.*, 2004]. The geochemical signature of such a hypothetical setting predating the current greenhouse climate era and stagnant lid regime is most likely to be preserved in tessera terrain and would manifest as low emissivity at 1 μm due to the low content of FeO and high SiO_2 content [*Hashimoto and Sugita*, 2003; *Hashimoto et al.*, 2008].

[67] The qualitative result of relative low thermal emission flux above tessera terrain does not dictate the conclusion of granitic surface composition. Absolute surface emissivity is not known and not also very conclusive even if known at only one wavelength. Other materials can have a significantly lower emissivity at 1 μm than basalt. Anorthosite rock is to 90 to 100% composed of the feldspars anorthite and albite, which both have reflectances at 1 μm of about 0.8. Anorthosite maybe even more plausible an explanation for low emissivity regions than granitic composition since its creation has less prerequisites. Anorthositic crust is supposed to differentiate on the top of a fully molten planetary mantle of terrestrial composition [*Taylor*, 1974]. In this case the situation on Venus would resemble the lunar crustal dichotomy of bright anorthosite highlands and dark basalt mares [*Nikolaeva et al.*, 1992].

[68] The negative flux anomaly observed here is not perfectly aligned with tessera boundaries, see Figure 12. This does not preclude an interpretation of tessera terrain to be mainly composed of less dense felsic material. Basaltic material might have been emplaced by volcanism, accretion of terranes or obduction on the buoyant and thickened crustal block. The basaltic material then would have undergone the same tectonic deformation history characteristic of tessera while the isostatically elevated topography prevented burial by lava floods. On the other hand buried granitic material might undergo remelting leading to felsic volcanism outside of tessera boundaries.

[69] However, there are serious concerns to the hypothesis of felsic tessera terrain. Aeolian transport of crater ejecta is known to occur on Venus. Finer grained ejecta and volcanic ash will be transported over larger distances. It is difficult to imaging that over time period of several Ga, that are required for either anorthosite or granites hypotheses, the tesserae had not been covered by a blanket of material closer to average composition. *Basilevsky et al.* [1997] gives an resurfacing rate of 0.1 to 10 cm per Ma from the fading of radar bright decimeter to decameter ejecta. Though higher winds at higher altitudes might sweep the tessera highlands [*Basilevsky et al.*, 1992] and tectonic deformation may expose the rock below compacted soil, compositional mixing of surface materials will be more relevant for areas significantly older than the relatively young plains and volcanic features.

[70] A second and more serious concern is that radar altimetry seems to be less reliable over tessera terrain, with a bias toward lower than actual surface altitudes. Figure 14 shows Magellan SAR mosaic and global topography data

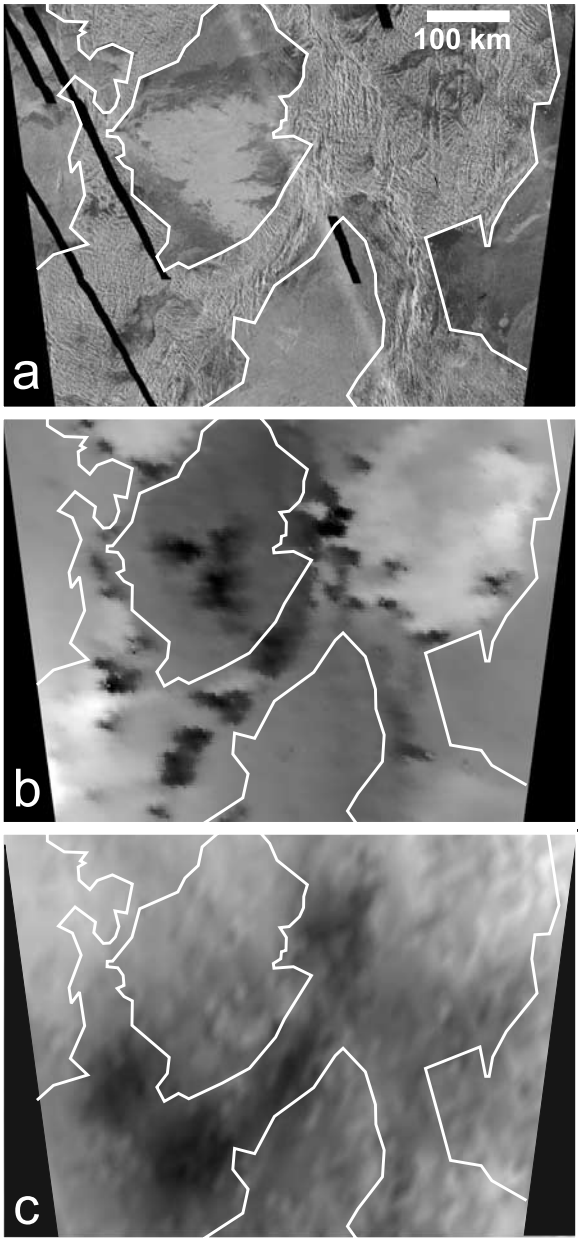

Figure 14. Qualitative comparison of different data sets in the Cocomama tessera region, sinusoidal projection from 66° to 60°S and 13° to 30°E. (a) Magellan left-look SAR (image data from NASA/JPL/Magellan). (b) Magellan GTDR altimetry (image data from NASA/JPL/Magellan). (c) VIRTIS thermal flux anomaly. Outlined is the boundary between mostly pristine plains and areas dominated by tectonic deformation. Deformed terrain is mostly tessera, the central and southeastern region with predominant north–south strike is characterized in electronic maps by *Tanaka et al.* [1997] as ridge belt. Magellan GTDR possibly has a bias to too low values over deformed areas. tessera-SAR-GTDR.

record GTDR of Cocomama tessera. Both seem difficult to reconcile with each other. The easternmost part of the tessera terrain is elevated above the surrounding plains. The deformed terrain encircling the smooth, nearly undeformed plain slightly northeast of the center of the image, is partly depressed relative to the plains. Emplacement of the plains without covering the depressed terrain seems improbable. Further support for the hypothesis of systematically too low radar altimetry is given by the negative NIR flux anomaly, that is in shape similar to the suspicious depressions, see Figure 14. The eastern, elevated block of tessera shows nonuniform flux anomaly. Isolated depressions circling the southern and western rim of the elevated tessera block have lower altimetry readings than embaying plains. Assuming that these readings are too low, smearing of Magellan altimetry with a 100 km FWHM gaussian weight function during data processing will lead to a diffuse, crescent shaped negative flux anomaly along the southern border of the tessera. Such a flux anomaly is observed. Similar considerations can be made for the other negative flux anomalies in the area. Magellan altimetry of tessera terrain needs to be examined more closely before any definite conclusions on emissivity of tessera can be made.

[71] Independent examination with a different approach analyzing VMC images did not reveal NIR contrast in the shape of tessera terrains (Basilevsky et al., submitted manuscript, 2008). Such contrast would be expected if these terrains were fully composed of anorthositic outcrops with an emissivity of 0.5.

6.2. Large Scale Ultramafic Volcanism

[72] The high thermal flux over young volcanic flows associated with coronae in Lada terra and less clearly over the nearby Lavinia basin might indicate a composition more mafic than the average plains, which are here used to define normal thermal flux. Most evidence, from morphology and in situ measurements, hints to a basaltic composition of plains [*Grimm and Hess*, 1997]. Basalts are created by partial melting of ultramafic mantle material, the amount of refractory mafic minerals in the liquid phase is determined by temperature and pressure conditions. The cratering record indicates that the most of the plains were created during an episode of increased resurfacing with little magmatic activity afterward [*Schaber et al.*, 1992; *Strom et al.*, 1994; *Basilevsky et al.*, 1997]. *Parmentier and Hess* [1992] furthermore propose that the upper mantle below the crust is depleted of felsic minerals and FeO through basalt generation during the resurfacing event. The depleted mantle material is assumed compositionally buoyant and not partaking in convection. *Head et al.* [1994] argue that pressure release melting in mantle diapirs at the base of this layer might produce large volumes of ultramafic, MgO-rich magma that might account for the large low-viscosity lava flows.

[73] Terrestrial analogues are komatiite or picrite that have been proposed by *Komatsu et al.* [1993] as lavas that could thermally erode basaltic surface and thus produce the incised sinuous channels found, e.g., on the young lava flows in or close to Quetzalpetlatl corona. These sinuous rilles are north of and with flow direction away from the thermal flux anomaly seen on the southern flank of Quetzalpetlatl. The mapping of *Komatsu et al.* [1993] does, however, not extend below 70°S which is unfortunately also the northern rim of the flux anomaly. The lava flows on the rim of Lavinia planitia feature simple and complex channels

with flow margins that share some characteristics with sinuous rilles but do not necessarily require thermal erosion [*Baker et al.*, 1997].

[74] The Lada-Lavinia regio, which features the most prominent thermal flux anomalies, has been characterized by *Magee and Head* [1995] as geological setting favorable for the generation of melt. Mantle downwelling below the Lavinia planitia basin is thought to be associated with the extensional Lada rift on the southern and eastern rim of Lavinia [*Baer et al.*, 1994]. The lava flows with anomalous IR flux are in the vicinity of coronae. Coronae are interpreted to be imprints of diapir activity and possibly linked to extensional rifting [*Stofan et al.*, 1997]. *Smrekar and Stofan* [1997] modeled the range of topographic signatures of coronae as result of an evolutionary process starting from an upwelling mantle plume, its cessation and as latest stage lithospheric delamination. *Elkins-Tanton et al.* [2007] modeled possible melt compositions in the context of lithosphere delamination and found, among others, ultramafic melts.

[75] Constraints on composition further than the assumption of a higher emissivity than that of basalt cannot be made with this simple atmospheric correction model, wherefore it might be idle to speculate on exact surface rock composition at this point. Furthermore the positive flux anomaly over Lavinia planitia is to some extent correlated with altimetry that given the empirical nature of this approach, rouses suspicions of systematical errors due to the assumption of an incorrect temperature. A similar error might pertain to the flux anomaly seen at volcanic edifices with a diameter in the magnitude of the assumed spatial resolution. Assumption of a lower spatial resolution, i.e., smoothing of the radar altimetry with a wider radius will lower the flux anomalies seen at these places.

[76] This is not true for the anomalies seen at the flank of topographic rises. The flux anomaly at the southern flank of Quetzalpetlatl is below 70°S, where VIRTIS images generally are affected by stray light. Also in considering the coverage plot (Figure 10) together with the usual viewing geometry of VIRTIS (the slit oriented parallel to the terminator) it becomes obvious that the Lavinia region has a certain bias to be observed at certain samples of the detector array. If the distribution of stray light on the detector array is not homogeneous the removal of stray light might lead to an systematic error that is not removed by averaging because the coverage of the southern hemisphere is not homogeneous. Further collection of data might resolve this issue.

7. Conclusions

[77] The atmospheric correction employed here and more importantly, the capability of VIRTIS on Venus Express to observe the same surface area repeatedly, provide consistent indications that some brightness variation in the 1.02 μm window cannot be accounted for by cloud transmittance and surface temperature depending only on altitude. Contrary to previous results in studies by *Lecacheux et al.* [1993] and *Meadows and Crisp* [1996], significant contrast, uncorrelated to cloud opacity and surface altitude, remains after atmospheric correction. The above statement owes much, if not everything, to the higher spatial resolution and area coverage achieved through the VIRTIS data set. The method employed here does not allow us to retrieve absolute surface emissivity, as it does not accurately address radiative transfer in the lowest atmosphere [*Hashimoto and Sugita*, 2003]. Furthermore the empirical determination of thermal flux to topography relation may lead to an error depending on distribution of surface emissivity with surface elevation; see *Hashimoto et al.* [2008] for evidence for such a distribution.

[78] Regardless of these intrinsic uncertainties, a relation exists between NIR flux and morphological units from Magellan radar images at medium altitudes. The lower than average flux over tessera terrain is possibly indicative of felsic composition such as granite or anorthosite, which have been suggested to exist on Venus by *Taylor and Campbell* [1983], *Nikolaeva et al.* [1992], and *Hashimoto and Sugita* [2003]. A similar observation and interpretation based on Galileo NIMS data is made by *Hashimoto et al.* [2008], who find generally lower emissivity in the highlands. A systematical bias toward lower altitude values in the Magellan topography data set over the highly tectonized tessera terrain is also conceivable and consistent with this result. Comparison with other altimetry data sets, e.g., Pioneer Venus, Venera 15/16, and possibly topography derived from Magellan stereo radar imaging might help to resolve this issue.

[79] Higher than average flux is found at some volcanic edifices in Lada terra and Themis, Imdr, and Phoebe regions, the latter three classified as active hot spots by *Smrekar et al.* [1997]. Lavinia planitia is characterized by a anomalously high flux likely caused by systematic errors. The positive flux anomalies located on the flanks of Shulamite, Shiwanokia, and Quetzalpetlatl coronae, are difficult to attribute to any systematical problem. The Quetzalpetlatl anomaly is well correlated with the young lava flows Cavillaca and Juturna flucti. The high flux anomaly at young lava flows is consistent the hypothesis of large volume komatiite or picrite volcanism predicted by *Head et al.* [1994] as consequence of chemical differentiation of the upper mantle in the course of secondary crust formation. Another possible interpretation would be that lithospheric delamination in association with the Quetzalpetlatl-Boala corona formation [*Smrekar and Stofan*, 1997] produced the ultramafic lavas [*Elkins-Tanton et al.*, 2007] that lead to the increased NIR flux.

[80] Overall probability of these compositional interpretations is however difficult to estimate, as no absolute surface emissivity is retrieved. To retrieve emissivity, an improved model of radiative transfer has to be implemented similarly to the work of *Hashimoto et al.* [2008] or *Arnold et al.* [2008]. Crucial input parameters of radiative transfer models, e.g., continuum absorption coefficient, subcloud haze and even surface temperature are poorly constrained. Analysis of VIRTIS data together with Magellan altimetry data might improve knowledge on these parameters [*Carlson et al.*, 1993a]. When a reliable estimate of Venus surface emissivity is achieved, the next step has to be comparison with near infrared emissivity or laboratory samples measured at high temperatures. Little data exist yet on high temperature emissivity of minerals, but more will be hopefully available soon [*Maturilli et al.*, 2007; *Helbert and Maturilli*, 2008]. This comparison will constrain surface rock

composition if near infrared emissivity is not dominated by chemical weathering and volatile transport of minerals. In this case some knowledge on the nature of the high-altitude radiothermal emissivity will be gained if data coverage can sufficiently be extended to these regions.

[81] **Acknowledgments.** We thank S. Smrekar for an insightful discussion of the geology of Venus and also for kindly providing many suggestions for the improvement of language. We acknowledge the financial support for the VIRTIS instrument from ASI and CNES. A significant part of this work was made possible by a grant from the Wernher von Braun foundation (Germany). We are grateful to the whole VIRTIS on Venus Express team for providing this excellent data set.

References

Allen, D. A., and J. W. Crawford (1984), Cloud structure on the dark side of Venus, *Nature*, *307*, 222–224.

Arnold, G., R. Haus, D. Kappel, P. Drossart, and G. Piccioni (2008), Venus surface data extraction from VIRTIS/Venus Express measurements: Estimation of a quantitative approach, *J. Geophys. Res.*, *113*, E00B10, doi:10.1029/2008JE003087.

Baer, G., G. Schubert, D. L. Bindschadler, and E. R. Stofan (1994), Spatial and temporal relations between coronae and extensional belts, northern Lada Terra, Venus, *J. Geophys. Res.*, *99*, 8355–8369.

Baines, K. H., et al. (2000), Detection of sub-micron radiation from the surface of Venus by Cassini/VIMS, *Icarus*, *148*, 307–311, doi:10.1006/icar.2000.6519.

Baker, V. R., G. Komatsu, V. C. Gulick, and T. J. Parker (1997), Channels and valleys, in *Venus II: Geology, Geophysics, Atmosphere, and Solar Wind Environment*, edited by S. W. Bougher et al., pp. 757–793, Univ. of Ariz. Press, Tuscon.

Basilevsky, A. T., and J. W. Head (2003), The surface of Venus, *Rep. Prog. Phys.*, *66*, 1699–1734, doi:10.1088/0034-4885/66/10/R04.

Basilevsky, A. T., O. V. Nikolaeva, and R. O. Kuz'min (1992), Resurfacing, in *Venus Geology, Geochemistry, and Geophysics: Research Results From the USSR*, edited by V. L. Barsukov et al., pp. 153–160, Univ. of Ariz. Press, Tuscon.

Basilevsky, A. T., J. W. Head, G. G. Schaber, and R. G. Strom (1997), The resurfacing history of Venus, in *Venus II: Geology, Geophysics, Atmosphere, and Solar Wind Environment*, edited by S. W. Bougher et al., pp. 1047–1084, Univ. of Ariz. Press, Tuscon.

Carlson, R. W., et al. (1991), Galileo infrared imaging spectroscopy measurements at Venus, *Science*, *253*, 1541–1548.

Carlson, R. W., K. H. Baines, M. Girard, L. W. Kamp, P. Drossart, T. Encrenaz, and F. W. Taylor (1993a), Galileo/NIMS near-infrared thermal imagery of the surface of Venus, *Proc. Lunar Planet. Sci. Conf.*, *24th*, 253.

Carlson, R. W., L. W. Kamp, K. H. Baines, J. B. Pollack, D. H. Grinspoon, T. Encrenaz, P. Drossart, and F. W. Taylor (1993b), Variations in Venus cloud particle properties: A new view of Venus's cloud morphology as observed by Galileo Near-Infrared Mapping Spectrometer, *Planet. Space Sci.*, *41*, 477–485, doi:10.1016/0032-0633(93)90030-6.

Coradini, A., et al. (1998), VIRTIS: An imaging spectrometer for the Rosetta mission, *Planet. Space Sci.*, *46*, 1291–1304.

Crisp, D., and D. Titov (1997), The thermal balance of the Venus atmosphere, in *Venus II: Geology, Geophysics, Atmosphere, and Solar Wind Environment*, edited by S. W. Bougher et al., pp. 353–384, Univ. of Ariz. Press, Tuscon.

Crisp, D., D. A. Allen, D. H. Grinspoon, and J. B. Pollack (1991), The dark side of Venus: Near-infrared images and spectra from the Anglo-Australian Observatory, *Science*, *253*, 1263–1266.

Crisp, D., V. S. Meadows, B. Bézard, C. de Bergh, J.-P. Maillard, and F. P. Mills (1996), Ground-based near-infrared observations of the Venus nightside: 1.27-μm O_2 ($a\Delta_g$) airglow from the upper atmosphere, *J. Geophys. Res.*, *101*, 4577–4594.

Crisp, D., et al. (2002), Divergent evolution among Earth-like planets: The case for Venus exploration, in *The Future of Solar System Exploration (2003–2013): First Decadal Study Contributions*, edited by M. V. Sykes, *Astron. Soc. Pac. Conf. Ser.*, *272*, 5–34.

Donahue, T. M., and C. T. Russell (1997), The Venus atmosphere and ionosphere and their interaction with the solar wind: An overview, in *Venus II: Geology, Geophysics, Atmosphere, and Solar Wind Environment*, edited by S. W. Bougher et al., pp. 3–32, Univ. of Ariz. Press, Tuscon.

Drossart, P., et al. (2007), Scientific goals for the observation of Venus by VIRTIS on ESA/Venus express mission, *Planet. Space Sci.*, *55*, 1653–1672, doi:10.1016/j.pss.2007.01.003.

Elkins-Tanton, L. T., S. E. Smrekar, P. C. Hess, and E. M. Parmentier (2007), Volcanism and volatile recycling on a one-plate planet: Applications to Venus, *J. Geophys. Res.*, *112*, E04S06, doi:10.1029/2006JE002793.

Esposito, L. W., J.-L. Bertaux, V. Krasnopolsky, V. I. Moroz, and L. V. Zasova (1997), Chemistry of lower atmosphere and clouds, in *Venus II: Geology, Geophysics, Atmosphere, and Solar Wind Environment*, edited by S. W. Bougher et al., pp. 415–458, Univ. of Ariz. Press, Tuscon.

Fegley, B., Jr., G. Klingelhöfer, K. Lodders, and T. Widemann (1997), Geochemistry of surface-atmosphere interactions on Venus, in *Venus II: Geology, Geophysics, Atmosphere, and Solar Wind Environment*, edited by S. W. Bougher et al., pp. 591–636, Univ. of Ariz. Press, Tuscon.

Ford, P. G., and G. H. Pettengill (1992), Venus topography and kilometer-scale slopes, *J. Geophys. Res.*, *97*, 13,103–13,112.

Gierasch, P. J., et al. (1997), The general circulation of the Venus atmosphere: An assessment, in *Venus II: Geology, Geophysics, Atmosphere, and Solar Wind Environment*, edited by S. W. Bougher et al., pp. 459–500, Univ. of Ariz. Press, Tuscon.

Goody, R. M., and Y. L. Yung (1989), *Atmospheric Radiation: Theoretical Basis*, 2nd ed., Oxford Univ. Press, New York.

Grieger, B., N. I. Ignatiev, N. M. Hoekzema, and H. U. Keller (2004), Indication of a near surface cloud layer on Venus from reanalysis of Venera 13/14 spectrophotometer data, in *Planetary Probe Atmospheric Entry and Descent Trajectory Analysis and Science*, edited by A. Wilson, *Eur. Space Agency Spec. Publ.*, *544*, 63–70.

Grimm, R. E., and P. C. Hess (1997), The crust of Venus, in *Venus II: Geology, Geophysics, Atmosphere, and Solar Wind Environment*, edited by S. W. Bougher et al., pp. 1205–1244, Univ. of Ariz. Press, Tuscon.

Grinspoon, D. H., J. B. Pollack, B. R. Sitton, R. W. Carlson, L. W. Kamp, K. H. Baines, T. Encrenaz, and F. W. Taylor (1993), Probing Venus's cloud structure with Galileo NIMS, *Planet. Space Sci.*, *41*, 515–542, doi:10.1016/0032-0633(93)90034-Y.

Hansen, J. E., and J. W. Hovenier (1974), Nature of the Venus clouds as derived from their polarization, in *Exploration of the Planetary System*, edited by A. Woszczyk and C. Iwaniszewska, *Symp. Int. Astron. Union*, *65*, 197–200.

Hansen, J. E., and L. D. Travis (1974), Light scattering in planetary atmospheres, *Space Sci. Rev.*, *16*, 527–610.

Hansen, V. L., J. J. Willis, and W. B. Banerdt (1997), Tectonic overview and synthesis, in *Venus II: Geology, Geophysics, Atmosphere, and Solar Wind Environment*, edited by S. W. Bougher et al., pp. 797–844, Univ. of Ariz. Press, Tuscon.

Hashimoto, G. L., and Y. Abe (2005), Climate control on Venus: Comparison of the carbonate and pyrite models, *Planet. Space Sci.*, *53*, 839–848, doi:10.1016/j.pss.2005.01.005.

Hashimoto, G. L., and T. Imamura (2001), Elucidating the rate of volcanism on Venus: Detection of lava eruptions using near-infrared observations, *Icarus*, *154*, 239–243, doi:10.1006/icar.2001.6713.

Hashimoto, G. L., and S. Sugita (2003), On observing the compositional variability of the surface of Venus using nightside near-infrared thermal radiation, *J. Geophys. Res.*, *108*(E9), 5109, doi:10.1029/2003JE002082.

Hashimoto, G. L., M. Roos-Serote, S. Sugita, M. S. Gilmore, L. W. Kamp, B. Carlson, and K. Baines (2008), Galileo Near-Infrared Mapping Spectrometer (NIMS) data suggest felsic highland crust on Venus, *J. Geophys. Res.*, doi:10.1029/2008JE003134, in press.

Head, J. W., L. S. Crumpler, J. C. Aubele, J. E. Guest, and R. S. Saunders (1992), Venus volcanism: Classification of volcanic features and structures, associations, and global distribution from Magellan data, *J. Geophys. Res.*, *97*, 13,153–13,197.

Head, J. W., E. M. Parmentier, and P. C. Hess (1994), Venus: Vertical accretion of crust and depleted mantle and implications for geological history and processes, *Planet. Space Sci.*, *42*, 803–811, doi:10.1016/0032-0633(94)90061-2.

Helbert, J., and A. Maturilli (2008), The heat is on: In the planetary emissivity laboratory, *Proc. Lunar Planet. Sci. Conf.*, *39th.*, 2408.

Helbert, J., N. Müller, P. Kostama, L. Marinangeli, G. Piccioni, and P. Drossart (2008), Surface brightness variations seen by VIRTIS on Venus Express and implications for the evolution of the Lada Terra region, Venus, *Geophys. Res. Lett.*, *35*, L11201, doi:10.1029/2008GL033609.

Ivanov, M. A., and J. W. Head (1996), Tessera terrain on Venus: A survey of the global distribution, characteristics, and relation to surrounding units from Magellan data, *J. Geophys. Res.*, *101*, 14,861–14,908.

Ivanov, M. A., and J. W. Head (2001), Geologic map of the Lavinia Planitia Quadrangle (V-55), Venus, *U.S. Geol. Surv. Geol. Invest. Map I-2684*.

Ivanov, M. A., and J. W. Head (2006), Geologic map of the Mylitta Fluctus Quadrangle (V-61), Venus, *U.S. Geol. Surv. Sci. Invest. Map I-2920*.

Kamp, L. W., F. W. Taylor, and S. B. Calcutt (1988), Structure of Venus's atmosphere from modelling of night-side infrared spectra, *Nature*, *336*, 360–362, doi:10.1038/336360a0.

Kargel, J. S., G. Komatsu, V. R. Baker, and R. G. Strom (1993), The volcanology of Venera and VEGA landing sites and the geochemistry of Venus, *Icarus*, *103*, 253–275, doi:10.1006/icar.1993.1069.

Kaula, W. M., and R. J. Phillips (1981), Quantitative tests for plate tectonics on Venus, *Geophys. Res. Lett.*, *8*, 1187–1190.

Knollenberg, R. G., and D. M. Hunten (1980), The microphysics of the clouds of Venus: Results of the Pioneer Venus particle size spectrometer experiment, *J. Geophys. Res.*, *85*, 8039–8058.

Komatsu, G., V. R. Baker, V. C. Gulick, and T. J. Parker (1993), Venusian channels and valleys: Distribution and volcanological implications, *Icarus*, *102*, 1–25, doi:10.1006/icar.1993.1029.

Kratter, K. M., L. M. Carter, and D. B. Campbell (2007), An expanded view of Lada Terra, Venus: New Arecibo radar observations of Quetzalpetlatl Corona and surrounding flows, *J. Geophys. Res.*, *112*, E04008, doi:10.1029/2006JE002722.

Lecacheux, J., P. Drossart, P. Laques, F. Deladerriere, and F. Colas (1993), Detection of the surface of Venus at 1.0 micrometer from ground-based observations, *Planet. Space Sci.*, *41*, 543–549, doi:10.1016/0032-0633(93)90035-Z.

Magee, K. P., and J. W. Head (1995), The role of rifting in the generation of melt: Implications for the origin and evolution of the Lada Terra-Lavinia Planitia region of Venus, *J. Geophys. Res.*, *100*, 1527–1552.

Marcq, E., T. Encrenaz, B. Bézard, and M. Birlan (2006), Remote sensing of Venus' lower atmosphere from ground-based IR spectroscopy: Latitudinal and vertical distribution of minor species, *Planet. Space Sci.*, *54*, 1360–1370, doi:10.1016/j.pss.2006.04.024.

Marov, M. I., V. E. Lystsev, V. N. Lebedev, N. L. Lukashevich, and V. P. Shari (1980), The structure and microphysical properties of the Venus clouds: Venera 9, 10, and 11 data, *Icarus*, *44*, 608–639, doi:10.1016/0019-1035(80)90131-1.

Maturilli, A., J. Helbert, and L. Moroz (2007), The Berlin Emissivity Database (BED): A collection of emissivity spectra for planetary analogue minerals, *Proc. Lunar Planet. Sci. Conf.*, *38th*, 1281.

Meadows, V. S., and D. Crisp (1996), Ground-based near-infrared observations of the Venus nightside: The thermal structure and water abundance near the surface, *J. Geophys. Res.*, *101*, 4595–4622.

Moroz, V. I. (2002), Estimates of visibility of the surface of Venus from descent probes and balloons, *Planet. Space Sci.*, *50*, 287–297.

Moroz, V. I., A. P. Ekonomov, B. E. Moshkin, H. E. Revercomb, L. A. Sromovsky, and J. T. Schofield (1985), Solar and thermal radiation in the Venus atmosphere, *Adv. Space Res.*, *5*, 197–232, doi:10.1016/0273-1177(85)90202-9.

Nikolaeva, O. V., M. A. Ivanov, and V. K. Borozdin (1992), Evidence on the crustal dichotomy, in *Venus Geology, Geochemistry, and Geophysics: Research Results From the USSR*, edited by V. L. Barsukov et al., pp. 129–139, Univ. of Ariz. Press, Tuscon.

Parmentier, E. M., and P. C. Hess (1992), Chemical differentiation of a convecting planetary interior: Consequences for a one plate planet such as Venus, *Geophys. Res. Lett.*, *19*, 2015–2018.

Pettengill, G. H., P. G. Ford, W. T. K. Johnson, R. K. Raney, and L. A. Soderblom (1991), Magellan: Radar performance and data products, *Science*, *252*, 260–265.

Pettengill, G. H., P. G. Ford, and R. J. Wilt (1992), Venus surface radiothermal emission as observed by Magellan, *J. Geophys. Res.*, *97*, 13,091–13,102.

Pettit, E., and S. B. Nicholson (1955), Temperatures on the bright and dark sides of Venus, *Publ. Astron. Soc. Pac.*, *67*, 293–303.

Phillips, R. J., R. F. Raubertas, R. E. Arvidson, I. C. Sarkar, R. R. Herrick, N. Izenberg, and R. E. Grimm (1992), Impact craters and Venus resurfacing history, *J. Geophys. Res.*, *97*, 15,923–15,948.

Pollack, J. B., et al. (1993), Near-infrared light from Venus' nightside: A spectroscopic analysis, *Icarus*, *103*, 1–42, doi:10.1006/icar.1993.1055.

Ragent, B., L. W. Esposito, M. G. Tomasko, M. I. Marov, and V. P. Shari (1985), Particulate matter in the Venus atmosphere, *Adv. Space Res.*, *5*, 85–115, doi:10.1016/0273-1177(85)90199-1.

Rappaport, N. J., A. S. Konopliv, A. B. Kucinskas, and P. G. Ford (1999), An improved 360 degree and order model of Venus topography, *Icarus*, *139*, 19–31, doi:10.1006/icar.1999.6081.

Sagan, C. (1962), Structure of the lower atmosphere of Venus, *Icarus*, *1*, 151–169, doi:10.1016/0019-1035(62)90015-5.

Saunders, R. S., R. E. Arvidson, J. W. Head, G. G. Schaber, E. R. Stofan, and S. C. Solomon (1991), An overview of Venus geology, *Science*, *252*, 249–252.

Schaber, G. G., et al. (1992), Geology and distribution of impact craters on Venus: What are they telling us?, *J. Geophys. Res.*, *97*, 13,257–13,301.

Seiff, A. (1983), Thermal structure of the atmosphere of Venus, in *Venus*, edited by D. M. Hunten and M. S. Matthews, pp. 215–279, Univ. of Ariz. Press, Tuscon.

Seiff, A. (1987), Further information on structure of the atmosphere of Venus derived from the VEGA Venus balloon and lander mission, *Adv. Space Res.*, *7*, 323–328, doi:10.1016/0273-1177(87)90239-0.

Seiff, A., J. T. Schofield, A. J. Kliore, F. W. Taylor, and S. S. Limaye (1985), Models of the structure of the atmosphere of Venus from the surface to 100 kilometers altitude, *Adv. Space Res.*, *5*, 3–58, doi:10.1016/0273-1177(85)90197-8.

Smrekar, S. E., and R. J. Phillips (1991), Venusian highlands: Geoid to topography ratios and their implications, *Earth Planet. Sci. Lett.*, *107*, 582–597, doi:10.1016/0012-821X(91)90103-O.

Smrekar, S. E., and E. R. Stofan (1997), Coupled upwelling and delamination: A new mechanism for coronae formation and heat loss on Venus, *Science*, *277*, 1289–1294.

Smrekar, S. E., W. S. Kiefer, and E. R. Stofan (1997), Large volcanic rises on Venus, in *Venus II: Geology, Geophysics, Atmosphere, and Solar Wind Environment*, edited by S. W. Bougher et al., pp. 845–878, Univ. of Ariz. Press, Tuscon.

Snyder, D. (2002), Cooling of lava flows on Venus: The coupling of radiative and convective heat transfer, *J. Geophys. Res.*, *107*(E10), 5080, doi:10.1029/2001JE001501.

Solomatov, V. S., and L.-N. Moresi (1996), Stagnant lid convection on Venus, *J. Geophys. Res.*, *101*, 4737–4754.

Solomon, S. C., et al. (1992), Venus tectonics: An overview of Magellan observations, *J. Geophys. Res.*, *97*, 13,199–13,255.

Spohn, T. (1991), Mantle differentiation and thermal evolution of Mars, Mercury, and Venus, *Icarus*, *90*, 222–236, doi:10.1016/0019-1035(91)90103-Z.

Stein, C., J. Schmalzl, and U. Hansen (2004), The effect of rheological parameters on plate behaviour in a self-consistent model of mantle convection, *Phys. Earth Planet. Inter.*, *142*, 225–255, doi:10.1016/j.pepi.2004.01.006.

Stevenson, D. J., T. Spohn, and G. Schubert (1983), Magnetism and thermal evolution of the terrestrial planets, *Icarus*, *54*, 466–489, doi:10.1016/0019-1035(83)90241-5.

Stofan, E. R., V. L. Sharpton, G. Schubert, G. Baer, D. L. Bindschadler, D. M. Janes, and S. W. Squyres (1992), Global distribution and characteristics of coronae and related features on Venus: Implications for origin and relation to mantle processes, *J. Geophys. Res.*, *97*, 13,347–13,378.

Stofan, E. R., V. E. Hamilton, D. M. Janes, and S. E. Smrekar (1997), Coronae on Venus: Morphology and origin, in *Venus II: Geology, Geophysics, Atmosphere, and Solar Wind Environment*, edited by S. W. Bougher et al., pp. 931–965, Univ. of Ariz. Press, Tuscon.

Stone, P. H. (1975), The dynamics of the atmosphere of Venus, *J. Atmos. Sci.*, *32*, 1005–1016.

Strom, R. G., G. G. Schaber, and D. D. Dawsow (1994), The global resurfacing of Venus, *J. Geophys. Res.*, *99*, 10,899–10,926.

Surkov, I. A., L. P. Moskaleva, V. P. Khariukova, A. D. Dudin, and G. G. Smirnov (1986), Venus rock composition at the VEGA 2 landing site, *J. Geophys. Res.*, *91*, 215–218.

Surkov, I. A., F. F. Kirnozov, V. N. Glazov, A. G. Dunchenko, and L. P. Tatsy (1987), Uranium, thorium, and potassium in the Venusian rocks at the landing sites of VEGA 1 and 2, *J. Geophys. Res.*, *92*, 537–540.

Surkov, Y. A., and V. L. Barsukov (1985), Composition, structure and properties of Venus rocks, *Adv. Space Res.*, *5*, 17–29, doi:10.1016/0273-1177(85)90237-6.

Svedhem, H., et al. (2007), Venus Express-The first European mission to Venus, *Planet. Space Sci.*, *55*, 1636–1652, doi:10.1016/j.pss.2007.01.013.

Tanaka, K. L., D. A. Senske, M. Price, and R. L. Kirk (1997), Physiography, geomorphic/geologic mapping and stratigraphy of Venus, in *Venus II: Geology, Geophysics, Atmosphere, and Solar Wind Environment*, edited by S. W. Bougher et al., pp. 667–694, Univ. of Ariz. Press, Tuscon.

Taylor, F. W. (2006), Venus before Venus Express, *Planet. Space Sci.*, *54*, 1249–1262, doi:10.1016/j.pss.2006.04.031.

Taylor, F. W., D. Crisp, and B. Bézard (1997), Near-infrared sounding of the lower atmosphere of Venus, in *Venus II: Geology, Geophysics, Atmosphere, and Solar Wind Environment*, edited by S. W. Bougher et al., pp. 325–351, Univ. of Ariz. Press, Tuscon.

Taylor, S. R. (1974), Geochemical evolution of the Moon, *LPI Contrib.*, *195*, 7–9.

Taylor, S. R. (1989), Growth of planetary crusts, *Tectonophysics*, *161*, 147–156.

Taylor, S. R., and I. H. Campbell (1983), No water, no granites: No oceans, no continents, *Geophys. Res. Lett.*, *10*, 1061–1064.

Titov, D. V., et al. (2006), Venus Express science planning, *Planet. Space Sci.*, *54*, 1279–1297, doi:10.1016/j.pss.2006.04.017.

Tsang, C. C. C., P. G. J. Irwin, F. W. Taylor, and C. F. Wilson (2008), A correlated-k model of radiative transfer in the near-infrared windows of venus, *J. Quant. Spectrosc. Radiat. Transfer*, *109*, 1118–1135, doi:10.1016/j.jqsrt.2007.12.008.

Turcotte, D. L. (1993), An episodic hypothesis for venusian tectonics, *J. Geophys. Res.*, *98*, 17,061–17,068.

von Zahn, U., S. Kumar, H. Niemann, and R. Prinn (1983), Composition of the Venus atmosphere, in *Venus*, edited by D. M. Hunten and M. S. Matthews, pp. 299–340, Univ. of Ariz. Press, Tuscon.

Wood, J. A. (1997), Rock weathering on the surface of Venus, in *Venus II: Geology, Geophysics, Atmosphere, and Solar Wind Environment*, edited by S. W. Bougher et al., pp. 637–661, Univ. of Ariz. Press, Tuscon.

P. Drossart and S. Erard, LESIA, Observatoire de Paris, 61 Avenue Observatoire, F-75014 Paris, France.

G. L. Hashimoto, Laboratory for Earth and Planetary Atmospheric Science, Department of Earth and Planetary Sciences, 1-1 Rokkodai-cho, Kobe University, Kobe 657-8501, Japan.

J. Helbert and N. Mueller, Institute of Planetary Research, German Aerospace Center, Rutherfordstrasse 2, D-12489 Berlin, Germany. (nils.mueller@dlr.de)

G. Piccioni, IASF-INAF, via del fosso del cavaliere 100, Rome I-00133, Italy.

C. C. C. Tsang, Atmospheric, Oceanic, and Planetary Physics, Department of Physics, University of Oxford, Clarendon Laboratory, Parks Road, Oxford OX1 3PU, UK.